Dynamic analyses of operating offshore wind turbines including soil-structure interaction

Haoran Zuo, Kaiming Bi [*, 1], Hong Hao[*, 2]

Centre for Infrastructure Monitoring and Protection, School of Civil and Mechanical Engineering, Curtin University, Kent Street, Bentley, WA 6102, Australia

[*, 1] *Corresponding author;* [*, 2] *Principal corresponding author.*

E-mail address: haoran.zuo@postgrad.curtin.edu.au *(H. Zuo);* kaiming.bi@curtin.edu.au *(K. Bi);* hong.hao@curtin.edu.au *(H. Hao).*

ABSTRACT

In the dynamic analyses of offshore wind turbines subjected to the external vibration sources, the wind turbines are normally assumed in the parked condition and the blades are considered by a lumped mass located at the top of the tower. In reality, the geometrical characteristics and rotational velocity of the blades can directly influence the wind loads acting on the blades. Moreover, the centrifugal stiffness generated by the rotating blades can increase the stiffness and natural frequencies of the blades, which in turn can further affect the structural responses. The lumped mass model, therefore, may lead to inaccurate structural response estimations. On the other hand, monopile, a long hollow steel member inserting into the water and sea bed, is generally designed as the foundation of an offshore wind turbine. The soil-monopile interaction can further alter the vibration characteristics and dynamic responses of offshore wind turbines. In the present study, the dynamic responses of the modern NREL 5 MW wind turbine subjected to the combined wind and sea wave loadings are numerically investigated by using the finite element code ABAQUS. The blades are explicitly modelled and soil-structure interaction (SSI) is considered. The influences of operational condition and rotor velocity on the dynamic behaviours are systematically investigated. It is found that the responses of the wind turbine in the operating condition are much larger than those in the parked

condition; SSI can affect the tower vibrations substantially, while it has a negligible effect on the in-plane vibrations of the blades.

Keywords: Offshore wind turbine, operational condition, SSI, rotor velocity

Nomenclature

m_e	Effective mass of monopile	coh	Spatial coherency loss function
m_p	Physical mass of monopile	ω	Angular frequency in rad/s
m_a	Added mass of monopile	v_{app}	Apparent wave velocity
C_a	Added mass coefficient	f_{mean}	Mean wind drag force
A_p	Cross section area of monopile	v_{rel}, v_f	Relative and fluctuating wind velocities
ρ_w	Sea water density	Ω	Rotor velocity
f_y	Yield strength	a, a'	Axial and tangential induction factors
ε_1, ε_2	Elastic and total strains	r	Radial distance from hub centre
Z_R	Transition depth	t_s	Time in sec
Z	Depth below sea bed	H_{hub}	Height of hub
s_u	Undrained shear strength of soil	θ	Phase difference between blades
d_P	Outer diameter of monopile	p_l, p_d	Local lift and drag forces on blade
γ'	Effective unit weight of soil	l	Chord length
J	Empirical constant	C_{lb}	Lift coefficient of blade
p, p_u	Lateral force and ultimate lateral soil resistance per unit length of monopile	C_{db}	Drag coefficient of blade
		α, β	Attack and pitch angles
		κ, φ	Pre-twist and flow angles
y	Lateral displacement of monopile	p_t, p_n	Local wind loads in the directions parallel and perpendicular to rotor plane
y_c	Deformation corresponding to one-half of the ultimate soil resistance	F_t, F_n	In-plane and out-of-plane wind loads on blade
ε_c	Strain corresponding to one-half of the maximum stress	R	Rotor radius
z	Axial deflection of monopile	$\phi_{e,1}$	First edgewise mode shape of blade
z_{peak}	Displacement corresponding to the maximum soil-monopile adhesion	$\phi_{f,1}$	First flapwise mode shape of blade
t, t_{max}	Mobilized and maximum soil-monopile adhesion	η	Sea surface elevation
Q, Q_p	Mobilized and end bearing capacities	g	Gravitational acceleration
S_{vv}	Fluctuating wind velocity spectrum	γ	Peak enhancement factor
h	Height	α_P, σ	Constants in JONSWAP spectrum
f	Frequency in Hz	f_m	Peak wave frequency in Hz
$\bar{v}$	Mean wind velocity	v_{10}	Mean wind velocity at 10 m above sea surface
v_*	Friction velocity	F	Fetch length
c	Monin coordinate	Φ	Random phase angle
K	Von-Karman's constant	x_w, z_w	Horizontal and vertical coordinates
z_0	Roughness length	v_x, a_x	Velocity and acceleration of water particles
$S_{f,j}$	Modal fluctuating drag force spectrum	d_w	Water depth
C_{dt}	Drag coefficient of tower	H	Wave height
A	Area of tower exposed to wind	k_w	Sea wave number
ρ	Air density	T, λ	Wave period and length
ϕ_j	jth mode shape of tower	F_w	Sea wave load per unit length of monopile
$\hat{v}$	Average mean wind velocity	C_{dp}	Drag coefficient of monopile
D	Decay constant	C_m	Inertia coefficient of monopile

1. Introduction

Offshore wind turbines play an important role in producing electrical energy. Multi-megawatt offshore wind turbines with slender tower and large rotor are widely adopted in the state-of-the-art designs to more efficiently extract the vast wind energy resources. For example, the tower height and rotor radius of the modern NREL 5 MW horizontal axis wind turbine reach 87.6 m and 63 m respectively [1]. These flexible wind turbines are vulnerable to the external vibration sources. For example, wind and sea wave loadings, which are experienced constantly during the whole lifetime of an offshore wind turbine, can result in excessive vibrations to the structures. These adverse vibrations may compromise the wind energy output, cause the fatigue damage to the structural components, and even direct structural damage under extreme conditions. To ensure the safe and effective operations of these offshore wind turbines, it is important to accurately understand the dynamic behaviours when they are subjected to the external vibration loadings.

Extensive research works have been conducted by different researchers to investigate the dynamic behaviours of wind turbines under wind, sea wave and/or seismic loadings. To simplify the analysis, the wind turbines were normally assumed in the parked condition, and the blades were modelled as a lumped mass located at the top of the tower [2-8] by neglecting the geometrical configurations of the blades and the interaction between the tower and blades. In reality, the geometrical characteristics and rotational velocity of the blades can directly influence the wind loads acting on the blades [9]. Moreover, the geometry of the rotor can influence the vibration characteristics of the wind turbine especially when it is in the operating condition since the locations of the blades are changing periodically and the centrifugal stiffness generated by the rotating blades can increase the stiffness and the natural frequencies of the blades [10], which in turn can indirectly affect the dynamic responses of wind turbines. The simplified lumped mass model therefore may lead to the inaccurate structural response estimations.

To investigate the influence of blades on the dynamic behaviours of wind turbines, Prowell et al. [11], Kjørlaug and Kaynia [12] and Santangelo et al. [13] considered the geometrical characteristics of the blades and explicitly developed the finite element (FE) models of the blades in the seismic analyses of wind turbines. However, only the parked condition was considered in these studies, rotating induced

blades location changes and stiffness increment therefore were not considered. To investigate the dynamic behaviours of operating wind turbines, Prowell et al. [14] performed shaking table tests to investigate its seismic responses, additional damping in the fore-aft direction was observed compared to the parked condition. Some researchers simplified each blade as a single [15, 16] or two [17] degrees-of-freedom (DOF) system, and the structural responses were estimated by using the home-made programs (e.g. in MATLAB). A lot of mathematics are involved in the calculations, these methods are therefore not convenient for other researchers/engineers to use. Moreover, wind loads acting along the height of the tower and the length of the blades are inevitably different, hence the structural responses may not be realistically captured by these simplified models. Some other researchers modelled the wind turbines by using the commercially available software such as FAST (e.g. [18]) or validated their models against FAST [19]. The structural components can be explicitly developed and the blades rotation can be considered by using FAST. However, as indicated in the user's guide [20], FAST employs a combination of modal and multi-body dynamics formulations and models the blades and tower as flexible elements using a linear modal representation that assumes small deflections. In other words, FAST can only simulate the elastic response of wind turbines. Under the extreme loading conditions, the wind turbine may experience nonlinear deformations, which may not be realistically considered by FAST.

On the other hand, the monopile is widely designed as the foundation of offshore wind turbines due to its simplicity [21, 22]. A typical monopile is a long hollow steel member with 3-6 m outer diameter and 22-40 m length [6], inserting into the sea water and sea bed. It can be regarded as an extension of the wind turbine tower. For such a slender flexible foundation, the interaction between the monopile and the surrounding soil is inevitable and can reduce the vibration frequencies or even vibration modes of the structure, which in turn may further influence the dynamic behaviours of offshore structures [23]. Many numerical [24, 25] and experimental [26, 27] studies have been carried out to investigate the influence of SSI on the vibration characteristics of wind turbines. Andersen et al. [24] and Arany et al. [25] investigated the effect of soil uncertainty on the first natural frequency of offshore wind turbine; Lombardi et al. [26] and Bhattacharya and Adhikari [27] conducted laboratory tests on a scaled wind turbine model and found that the natural frequencies of wind turbine were

strongly related to the foundation flexibility. Some researchers also investigated the influence of soil-structure interaction (SSI) on the dynamic responses of wind turbines [6, 7, 12, 13, 16, 17, 21, 28]. However, it should be noted that in all these studies the wind turbines were either assumed in the parked condition [12, 13] and the blades were lumped at the tower top [6, 7, 28], or the rotation of the blades was considered by the simplified 1- or 2-DOF systems [16, 17, 21]. The influence of blades on the structural responses was therefore not realistically considered as discussed above.

In the present study, a detailed FE model of the modern NREL 5 MW wind turbine is developed by using the commercially available finite element code ABAQUS. The tower and blades are explicitly modelled. Compared to the previous simplified models, the present numerical model can realistically consider the influence of geometrical configurations of the blades on the wind loads, as well as the centrifugal stiffness variations of the blades generated by the blades rotation. Moreover, the possible nonlinear behaviour of the tower and blades can also be conveniently considered. This FE model can be readily used by other researchers/engineers. This detailed FE model is used to systematically investigate the influences of operational conditions and SSI on the wind turbine responses when subjected to the combined actions of wind and sea wave loadings. The structure of this paper is organized as follows: the NREL 5 MW wind turbine and the development of the FE model is presented in Section 2; Section 3 defines the vibration sources including the wind and sea wave loadings which are used in the analyses; the numerical results are discussed in Section 4 and some concluding remarks are made in Section 5.

2. Numerical model

2.1. NREL 5 MW wind turbine

The modern NREL 5 MW three-bladed wind turbine is selected as an example in the present study. The wind turbine is selected simply because its properties are well defined in many previous studies such as in [1]. The outer diameters at the top and bottom of the tower are 3.87 m and 6 m, and the corresponding wall thickness are 0.019 m and 0.027 m respectively. The outer diameter and wall thickness decrease linearly from the bottom to the tower top. The total length of the monopile is 75 m, in which 20 m and 45 m are in the water and sea bed respectively and another 10 m is above the mean

sea level [29]. The diameter and wall thickness of the monopile foundation are the same as the bottom cross section of the tower. The radius of the hub is 1.5 m and the length of the blade is 61.5 m. The distance from the hub centre to the tip of the blade is therefore 63 m.

The pre-twisted blade is made up of eight unique airfoil sections and the geometries can be found in [1]. The mass of each blade is 17,740 kg as reported [1], but the wall thickness of the blade is not given in [1]. A uniform wall thickness is assumed in the present study and a thickness of 0.019 m is computed to ensure that the mass of the blade is the same as that reported in [1]. Fig. 1 shows the main dimensions of the wind turbine and Table 1 tabulates the detailed information.

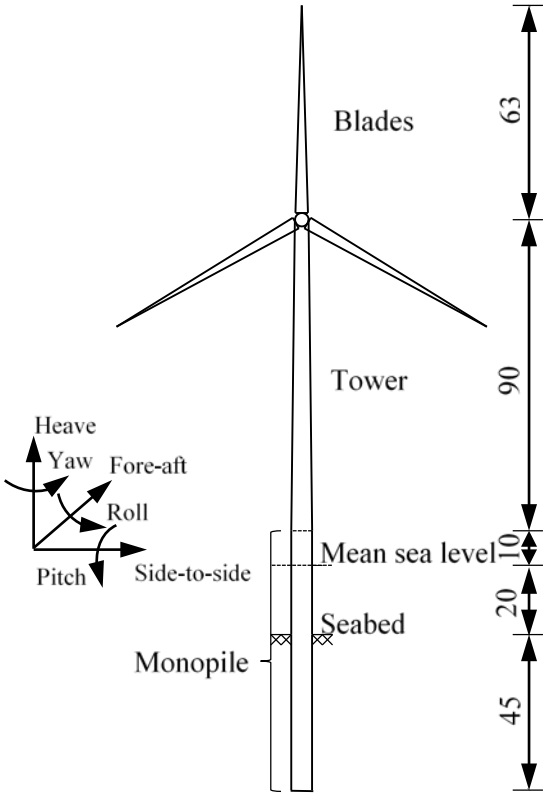

Fig. 1. Offshore wind turbine model (Front view, dimensions in m)

2.2. Finite element model

The detailed three-dimensional (3D) FE model of the NREL 5 MW wind turbine is developed by using the finite element code ABAQUS. The tower and monopile above and in the sea water are modelled by the shell elements (S4 in ABAQUS), while the monopile buried in the soil medium is

modelled by the beam elements (B31 in ABAQUS). The nacelle and hub are fixed at the top of the tower, only the masses of them are considered in the numerical model, and they are modelled by the point mass element in ABAQUS and is lumped at the tower top. To ensure the deformation continuity at the connection between the tower and the monopile, the cross sections of the bottom of the tower and the top of the monopile are tied with each other. To consider the influence of blades on the dynamic behaviours of offshore wind turbines, the blades are explicitly developed and they are modelled by the shell elements again. A hinge connection between the tower and blades is defined to simulate the rotation of the blades and the rotational DOF along the out-of-rotor-plane direction is released.

Table 1

Properties of NREL 5MW wind turbine [1]

NREL 5 MW baseline wind turbine properties		
Basic description	Max. rated power	5 MW
	Rotor orientation, configuration	Upwind, 3 blades
	Rotor diameter	126 m
	Hub height	90 m
	Cut-in, rated, cut-out wind speed*	3 m/s, 11.4 m/s, 25 m/s
Blade	Cut-in, rated rotor speed	6.9 rpm, 12.1 rpm
	Length	61.5 m
	Overall (integrated) mass	17,740 kg
	Structural damping ratio	0.48%
	Hub diameter	3 m
Hub and Nacelle	Hub mass	56,780 kg
	Nacelle mass	240,000kg
	Height above water	87.6 m
Tower	Overall (integrated) mass	347,460 kg
	Structural damping ratio	1%

*In Table 1, cut-in wind speed means that wind turbine starts to rotate at a (cut-in) rotor speed of 6.9 rpm; rated wind speed means the maximum energy output of wind turbine will be achieved at a (rated) rotor speed of 12.1 rpm and cut-out wind speed is the speed above which the wind turbine stops working in order to protect the electrical and mechanical components.

The cross sections of the blades, tower and monopile in the water are divided into 24 elements as suggested in [30]. A convergence test shows that an element size of 1 m along the blades, tower and monopile in the water and soil yields a good balance between the computational time and accuracy, an element size of 1 m is therefore selected in these directions. As mentioned above, the monopile above and in the sea water is modelled by the shell elements while the monopile in the soil is modelled by

155 the beam elements in order to conveniently consider SSI. To make sure the same deformations of the
156 beam element and shell elements at the sea bed level, the node of the beam element and nodes of the
157 shell elements are coupled with each other at this cross section. Fig. 2 shows FE model of the wind
158 turbine except the monopile in the soil medium, the modelling of which will be discussed in Section
159 2.3. In the numerical model, the three blades are labelled as #1 to #3 in an anticlockwise direction as
160 shown in Fig. 2.
161

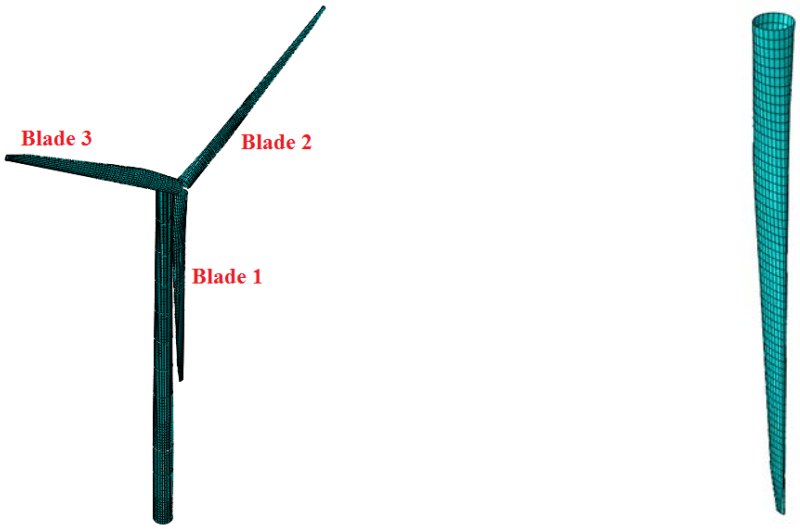

(a) Wind turbine in the parked condition (b) Blade

162 Fig. 2. FE model of the wind turbine (the monopile in the soil medium is not shown)
163

164 The blades are made of polyester with a density of 1850 kg/m^3 [31]. The tower and monopile are
165 made of steel. For the monopile above the mean sea level and buried in the soil medium, the density is
166 7850 kg/m^3, while the density of the tower is taken as 8500 kg/m^3 [1] to account for the paint, welds,
167 bolts and flanges that are not directly considered in the numerical model. For the monopile in the sea
168 water, the vibrating monopile can impart an acceleration to the surrounding sea water. The water-
169 monopile interaction is modelled by the added mass method (e.g. [30]) in the present study, in which
170 the effective mass m_e of the monopile can be expressed as

$$m_e = m_p + m_a \tag{1}$$

where m_p is the monopile physical mass and m_a denotes the added mass which can be calculated as [32]

$$m_a = C_a A_p \rho_w \quad (2)$$

where A_p is the cross section area of the monopile; ρ_w=1030 kg/m^3 is the sea water density and C_a is the added mass coefficient, which is assumed as 1.0 in the present study [32]. The effective density of the monopile in the sea water is therefore 8880 kg/m^3. Table 2 tabulates the material properties of the blades, tower and monopile. The polyester and steel are assumed as ideal elastic-plastic materials and the relationship between stress and strain is shown in Fig. 3. As shown in Fig. 3, f_y is the yield strength, ε_1 is the elastic strain and ε_2 is the strain which equals to the sum of the elastic and plastic strains.

Table 2

Material properties of the wind turbine [1, 31]

Component	Material	Density (kg/m^3)	Young's modulus (GPa)	Poisson's ratio	Yield strength (MPa)	Plastic strain
Blade	Polyester	1850	38	0.3	700	0.02
Tower	Steel	8500	210	0.3	235	0.01
Monopile in the water	Steel	8880	210	0.3	235	0.01
Monopile above water and in the soil	Steel	7850	210	0.3	235	0.01

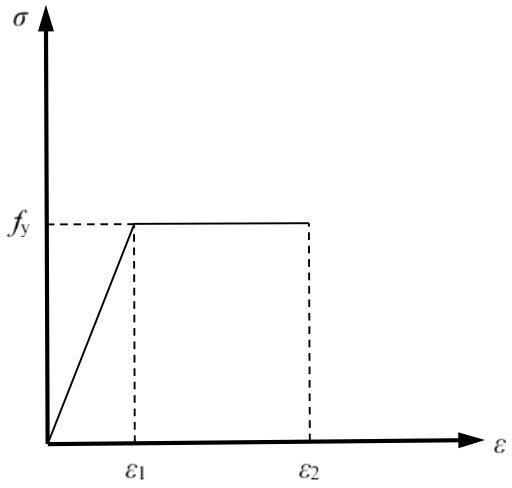

Fig. 3. The stress-strain relationship

187 Some previous studies (e.g. [1, 19]) calculated the vibration frequencies and vibration modes of the
188 NREL 5 MW wind turbine in the parked condition and without considering SSI. To examine the
189 accuracy of the developed FE model, the natural frequencies and vibration modes of the wind turbine
190 are calculated and compared with those in a previous study [1]. For a fair comparison, the parked
191 condition is considered and the bottom of the tower is fixed (i.e. SSI is not considered) in this section.
192 Table 3 tabulates the first 12 natural frequencies, the corresponding vibration modes and the
193 differences of the vibration frequencies between these two studies. It can be seen that in general good
194 agreements are observed. Slightly larger differences are obtained when the frequencies are
195 corresponding to the vibration modes of the blades. This is because the strengthening webs in the
196 blades are not included in the numerical model due to the lack of the detailed geometry and material
197 properties. The first flapwise and edgewise vibration mode shapes of the blade are compared with
198 those in another study [33] and the results are shown in Fig. 12 in Section 3.2. Good agreements are
199 obtained again and the slightly larger amplitudes in the present model are because the strengthening
200 webs are not modelled as discussed above.
201
202 **Table 3**
203 Natural frequencies of NREL 5 MW wind turbine in the parked condition and without considering SSI

Mode	Description	[1] (Hz)	Current study (Hz)	Difference
1	1st tower side-to-side	0.312	0.300	-3.85%
2	1st tower fore-aft	0.324	0.316	-2.47%
3	1st blade flapwise yaw	0.666	0.490	-26.43%
4	1st blade flapwise pitch	0.668	0.541	-19.01%
5	1st blade collective flap	0.699	0.607	-13.16%
6	1st blade edgewise pitch	1.079	1.172	8.62%
7	1st blade edgewise yaw	1.090	1.210	11.01%
8	2nd blade flapwise yaw	1.934	1.729	-10.60%
9	2nd blade flapwise pitch	1.922	1.970	2.50%
10	2nd blade collective flap	2.021	2.252	11.43%
11	2nd tower side-to-side	2.936	2.705	-7.87%
12	2nd tower fore-aft	2.900	2.855	-1.55%

204
205 **2.3. Soil springs**
206 As discussed above, the interaction between the monopile foundation and the surrounding soil may
207 significantly influence the dynamic behaviours of offshore wind turbine. To more accurately perform
208 dynamic analysis, SSI is considered in the present study. Many different methods have been adopted

by different researchers to consider SSI (e.g. [6, 12, 26]). Due to the simplicity and accuracy, the nonlinear soil springs are adopted in the present study.

In the nonlinear soil spring method, the lateral resistances of the soil against the foundation movements are depicted by the springs in the directions perpendicular and parallel to the rotor plane (the *p-y* springs in Fig. 4), and the vertical springs attached to the monopile are applied to simulate the shaft friction (*t-z* spring) and end bearing capacity at the tip of the monopile (*Q-z* spring). The space between each group of soil springs is selected as 1 m as suggested in [6], and they are modelled by the ground spring elements in ABAQUS. Fig. 4 shows the model of the monopile foundation attached with soil springs. The properties of the soil springs are described by the *p-y*, *t-z* and *Q-z* curves as recommended in API [34] and DNV-OS-J101 [35], which are briefly introduced in this section.

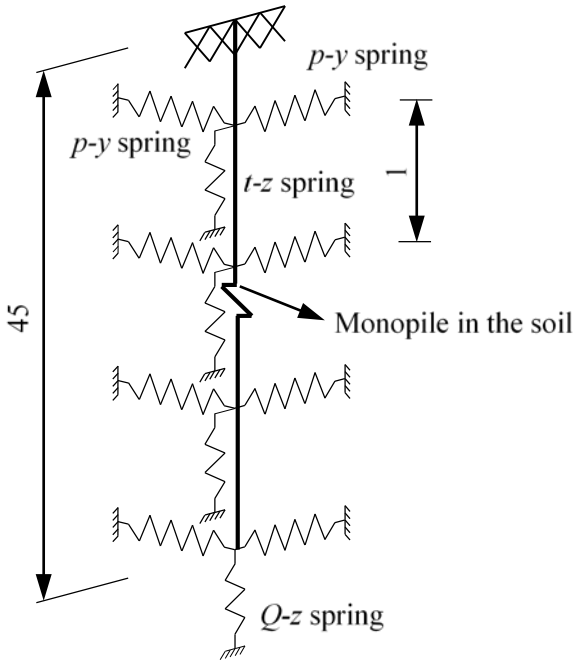

Fig. 4. SSI modelling (not to scale, dimensions in m)

In the present study, only the undrained clay is considered. As recommended in [34] and [35], the lateral force per unit length of the monopile (p) is related to the undrained shear strength of soil s_u and the transition depth Z_R which is expressed by

$$Z_R = 6s_u d_p/(\gamma' d_p + Js_u) \quad (3)$$

where d_p is the outer diameter of the monopile; γ' is the effective unit weight of soil and it is 8 kN/m^3 and J is a dimensionless empirical constant, and the value of 0.5 is adopted in the present study [6].

When $s_u \leq 100$ kPa and the depth below the sea bed $Z > Z_R$, the lateral force per unit length of the monopile can be calculated as

$$p = \begin{cases} 0.5p_u(y/y_c)^{1/3} & \text{for } y \leq 3y_c \\ 0.72p_u & \text{for } y > 3y_c \end{cases} \quad (4)$$

where y is the lateral displacement of the monopile and y_c is the deformation at which the strength of the soil reaches one-half of the ultimate soil resistance, which is estimated as

$$y_c = 2.5\varepsilon_c d_p \quad (5)$$

in which, ε_c is the strain corresponding to one-half of the maximum stress in laboratory undrained compression tests of undisturbed soil. The relationship between s_u and ε_c proposed by Ashour et al. [36] is used in the present study. Three soil undrained shear strengths (25, 50 and 100 kPa) are considered in this study, the corresponding values of ε_c are 0.02, 0.008 and 0.006 respectively.

In Eq. (4), p_u is the ultimate lateral soil resistance per unit length of the monopile, which can be calculated as

$$p_u = \begin{cases} (3s_u + \gamma' Z)d_p + Js_u Z & \text{for } 0 < Z \leq Z_R \\ 9s_u d_p & \text{for } Z > Z_R \end{cases} \quad (6)$$

When $Z \leq Z_R$, p becomes

$$p = \begin{cases} 0.5p_u(y/y_c)^{1/3} & \text{for } y \leq 3y_c \\ 0.72p_u(1-(1-Z/Z_R)(y-3y_c)/12y_c) & \text{for } 3y_c < y \leq 15y_c \\ 0.72p_u(Z/Z_R) & \text{for } y > 15y_c \end{cases} \quad (7)$$

The axial resistance of the soil is modelled by a combination of shaft friction and end bearing capacity at the monopile tip as shown in Fig. 4. The relationship between the mobilized soil-monopile shear transfer and monopile displacement at any depth can be represented by the *t*-*z* curve [34]. Similarly, *Q*-*z* curve is used to describe the relationship between the end bearing resistance and axial tip deflection [34]. In API [34], the t/t_{max} versus z/z_{peak} and Q/Q_p versus z/d_p relationships are tabulated. In which z is the monopile axial deflection at any depth below the sea bed; z_{peak} is the displacement corresponding to the maximum soil-monopile adhesion and the value of z_{peak} is typically 1% of the

monopile outer diameter d_p; t and t_{max} are the mobilized and maximum soil-monopile adhesion respectively; Q and Q_p are the mobilized and end bearing capacities respectively. The values of t_{max} and Q_p are dependent on the undrained soil shear strength s_u and can be calculated as suggested in [34]. Substituting t_{max}, z_{peak}, Q_p and d_p into the tables in [34], the t versus z and Q versus z relationships can be obtained.

Fig. 5 shows the p-y, t-z and Q-z curves at different depths (5 to 45 m with an increment of 10 m) below the sea bed with s_u=50 kPa (corresponds to a typical medium clay). As shown in Fig. 5(a), p is not influenced by the depth when it is larger than 25 m. Fig. 5 (c) shows the relationship at the monopile tip, the depth is fixed and therefore only one curve is included in Fig. 5 (c).

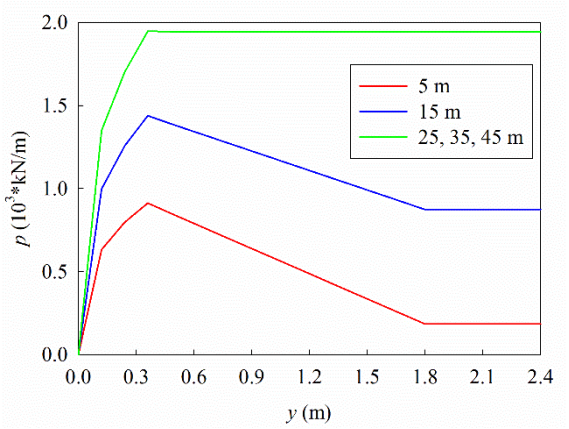

(a) p-y curve

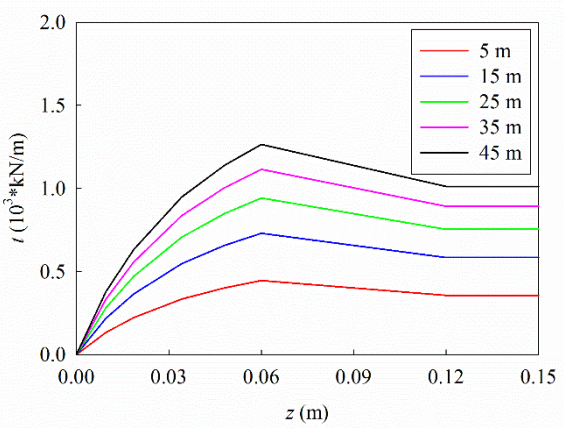

(b) t-z curve

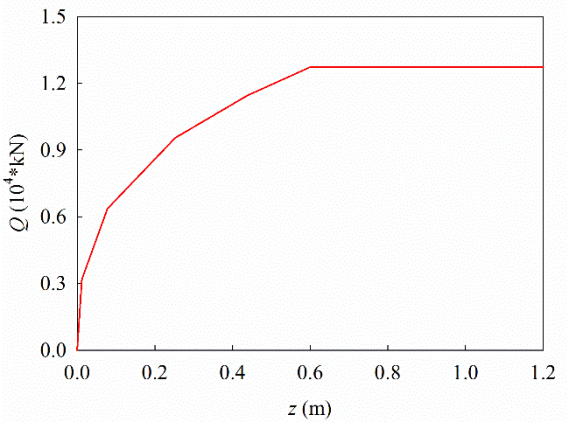

(c) Q-z curve

Fig. 5. The p-y, t-z and Q-z curves

2.4. Vibration characteristics

After the nonlinear soil springs are defined, the vibration frequencies and vibration modes of the wind turbine with the consideration of SSI are calculated. As discussed above, three undrained shear strengths of soil are considered in the present study. For conciseness, only the results when s_u=50 kPa are reported. Table 4 tabulates the first ten natural frequencies and Fig. 6 shows the corresponding vibration modes. To show the mode shape more clearly, the blades are not shown when the mode is dominated by the tower vibration.

Table 4

First ten natural frequencies of the wind turbine with SSI (s_u=50 kPa)

Mode	Description	f (Hz)
1	tower fore-aft (1st order)	0.154
2	tower side-to-side (1st order)	0.156
3	blade flapwise yaw (1st order)	0.474
4	blade flapwise pitch (1st order)	0.536
5	blade collective flap (1st order)	0.596
6	tower side-to-side (2nd order)	1.096
7	tower fore-aft (2nd order)	1.121
8	blade edgewise pitch (1st order)	1.206
9	blade edgewise yaw (1st order)	1.250
10	blade flapwise yaw (2nd order)	1.626

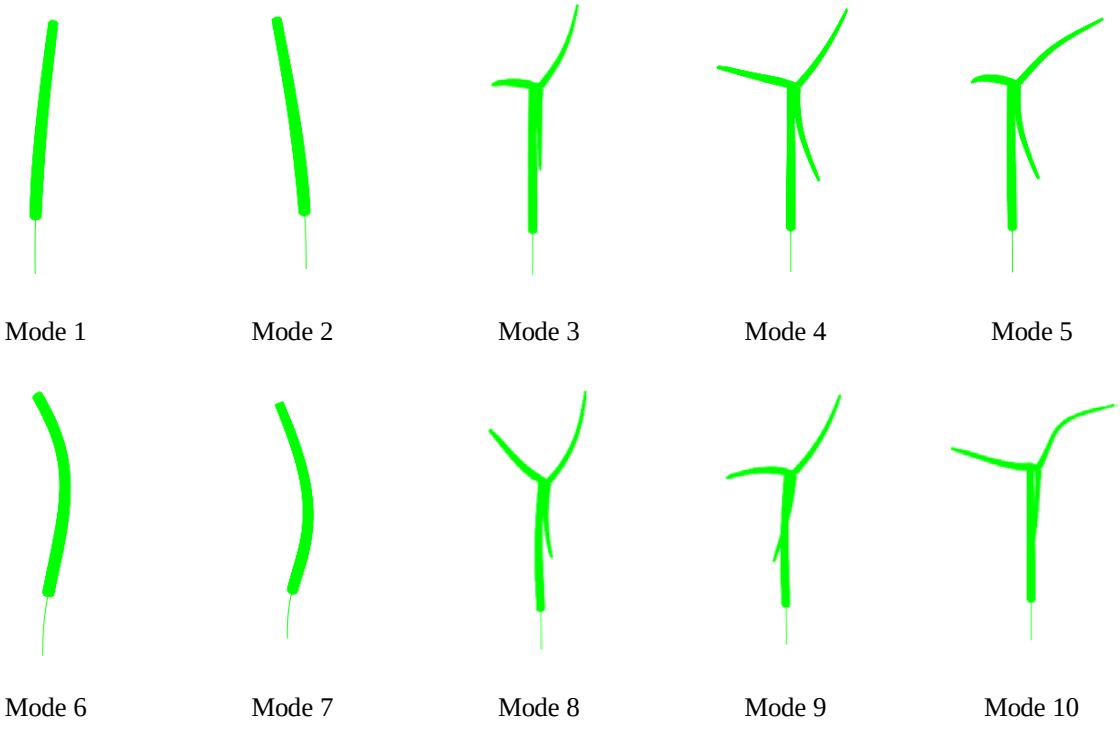

Fig. 6. Vibration modes of the wind turbine with SSI

2.5. Damping

The damping mechanism of offshore wind turbine is quite complicated and it normally comprises structural damping, aerodynamic damping, hydrodynamic damping and soil damping, which account for the contributions of the structure itself, wind, surrounding sea water and supporting soil respectively [25]. The structural damping ratios of the blades and the tower are 0.48% and 1% respectively as suggested in [1]. Aerodynamic damping results from the relative velocity between the wind and the rotating blades, which depends on the wind velocity, rotor speed, the geometrical configurations of the blades and the flow around the blades [37]. It is not easy to accurately obtain the aerodynamic damping. The aerodynamic damping in the fore-aft direction for an operating wind turbine is normally within the range of 1-6% [38]. Without loss of generality, a constant value of 3.5% is adopted in the present study as suggested by Bisoi and Haldar [6, 7]. For a parked wind turbine or in the side-to-side direction, previous studies (e.g. [25, 38]) revealed that the aerodynamic damping ratio is almost zero, and zero is adopted in the present study. The hydrodynamic damping results from the drag between the tower and the surrounding water. The upper limit of hydrodynamic damping ratio is about 0.23% [25] and this value is used in this study. The soil damping develops from SSI and it includes the material damping of the soil and the wave radiation damping which may go up to as high as 20% for the subgrade medium in some cases [6]. However, as will be demonstrated in Sections 3.1 and 3.3, the frequency contents of wind and sea wave loads are very low (up to 0.2 and 0.8 Hz respectively), and as indicated in [39] very little energy is dissipated by the radiation of waves when the excitation frequency is below 1 Hz, the wave radiation damping is therefore neglected in the numerical model. The material damping is thus dominant in the soil damping and 1% is assumed in the present study [25]. Therefore, summing all the components together, the damping ratio is 3.98% in the fore-aft direction for the rotating blades; for the parked blades or in the side-to-side direction, the value is 0.48%; and the damping ratio of the tower taking into account SSI is 2.23%. The damping of offshore wind turbine is considered by means of Rayleigh damping and the first out-of-plane and in-plane vibration frequencies of the tower and blades are used to calculate the mass and stiffness coefficients for the tower and blades respectively [40].

3. Vibration sources

In the present study, the wind and sea wave loadings, which are experienced during the whole lifetime of an offshore wind turbine, are considered as the external vibration sources. The wind and sea wave loads are stochastically simulated based on the sophisticated simulation techniques, and they are briefly introduced in this section for completeness of the paper.

3.1. Wind load on the tower

The wind load can be decomposed into a constant mean wind load and a fluctuating component. The Kaimal spectrum [10] is used to model the power spectral density (PSD) function of the fluctuating wind velocity along the tower, which is given by

$$S_{vv}(h,f) = \frac{v_*^2}{f}\frac{200c}{(1+50c)^{5/3}} \tag{8}$$

where

$$c = fh/\bar{v}(h) \tag{9}$$

and

$$\bar{v}(h) = v_* \ln(h/z_0)/K \tag{10}$$

in which h is the height of the location where wind load is calculated; f is the frequency in Hz; $\bar{v}$ is the mean wind velocity; v_* is the friction velocity; c is the Monin coordinate; K is the von-Karman's constant, which is generally taken as 0.4 [41] and z_0 is the roughness length.

For a continuous line-like structure, like the tower, the wind loads at different locations along the tower are different but with certain similarities, which is known as the spatial correlation effect. The spatial correlation effect is normally described by a spatial coherency loss function. The modal fluctuating drag force power spectrum, which considers the influence of spatial correlation effect, can be calculated by [10]

$$S_{f,j}(f) = (C_{dt}A\rho)^2 \sum_{k=1}^{N}\sum_{l=1}^{N} S_{v_k v_l}(f)\bar{v}_k\bar{v}_l\phi_j(k)\phi_j(l) \tag{11}$$

in which C_{dt} is the drag coefficient of the tower; A is the total area of the tower exposed to the wind; ρ is the air density; $\bar{v}_k$and $\bar{v}_l$ are the mean wind velocities at locations k and l respectively; $\phi_j(k)$ and $\phi_j(l)$

are the *j*th mode shape at locations *k* and *l*. As will be demonstrated in the following analysis, the energy of wind load mainly concentrates in the low frequency range (see Fig. 7) and normally the first vibration mode of the tower can be excited by the wind, *j*=1 is therefore used in the simulation. S_{vkvl} is the cross PSD function of wind velocity between locations *k* and *l*, which can be expressed as

$$S_{v_k v_l}(f) = \sqrt{S_{v_k v_k}(f) S_{v_l v_l}(f)}\, coh(k, l; f) \tag{12}$$

where S_{vkvk} and S_{vlvl} are the wind velocity auto PSDs as given by Eq. (8); $coh(k, l; f)$ is the spatial coherency loss function between locations *k* and *l* and the model as proposed by Huang et al. [42] is adopted in the present study

$$coh(k, l; f) = exp\left(-\frac{D\omega|k-l|}{2\pi\hat{v}}\right) exp\left(-i\frac{k-l}{v_{app}}\omega\right) \quad (k > l) \tag{13}$$

in which, $|k\text{-}l|$ and $\hat{v}$ are the distance and average mean wind velocity between locations *k* and *l* respectively; *D* is a decay constant; ω is angular frequency in rad/s and v_{app} is the apparent wave velocity. For $k<l$, the spatial coherency loss function is the complex conjugate of that with $k>l$.

The time histories of the fluctuating drag force with zero mean then can be simulated by using the Inverse Fast Fourier transform (IFFT) technique (e.g. [43, 44]).

The mean wind drag force can be calculated by

$$\bar{f}_{mean,i} = \frac{1}{2} C_{dt} A_i \rho \bar{v}_i^2 \tag{14}$$

in which, A_i and $\bar{v}_i$ are the area associated with location *i* and the mean wind velocity at location *i* respectively.

The wind loads at different locations along the tower are different. To simplify the analysis, the tower is divided into nine segments in the simulation and the drag force is assumed to be the same within each segment. The lengths of the top and bottom segments are 5 and 15 m respectively and other segments are 10 m length. The mean wind velocity at the top of the tower is taken as 15 m/s, and the roughness length, air density, drag coefficient, decay constant and apparent wave velocity are 0.005, 1.2 kg/m^3, 1.2, 0.04 and 10 m/s respectively. Fig. 7 shows the fluctuating wind velocity PSDs in segments S1 (85-90 m along the tower) and S5 (45-55 m) and the corresponding model values. The model and simulated coherency loss functions between segments S1and S5 are presented in Fig. 8. As

shown in Figs. 7 and 8, the simulated results are in well agreement with the corresponding model values. For brevity, not all the drag forces along the tower are shown. Only the time histories in two example segments (S1 and S5) are shown in Fig. 9.

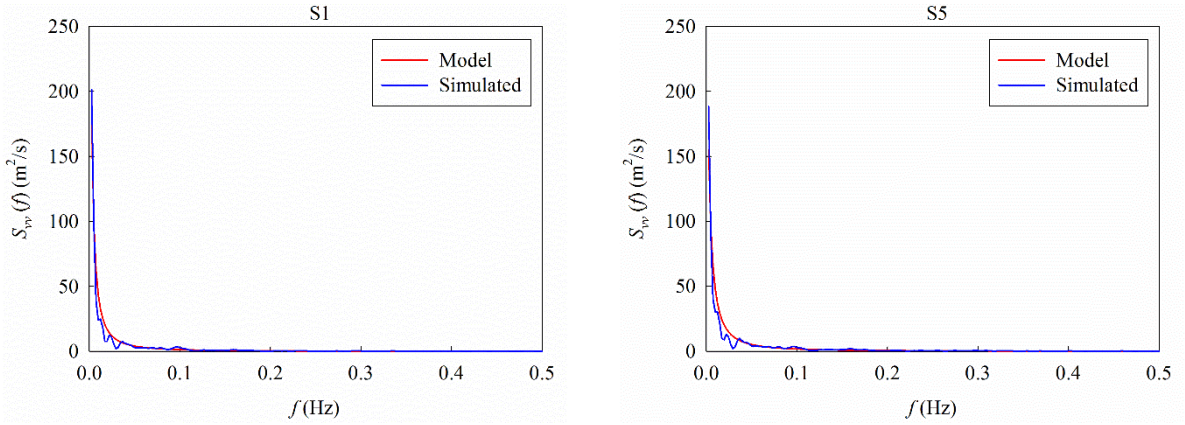

Fig. 7. Comparisons of the simulated wind velocity with the model PSDs

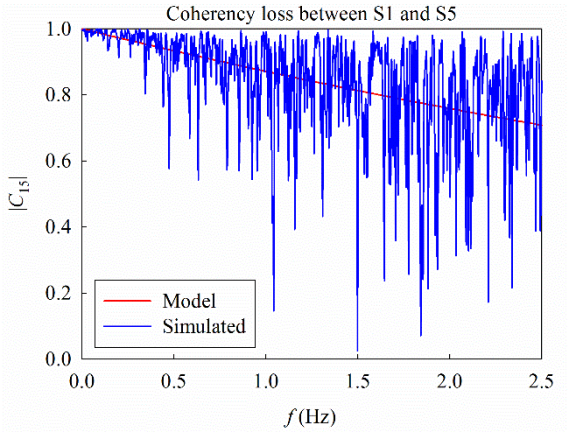

Fig. 8. Comparison between the simulated and model coherency loss functions

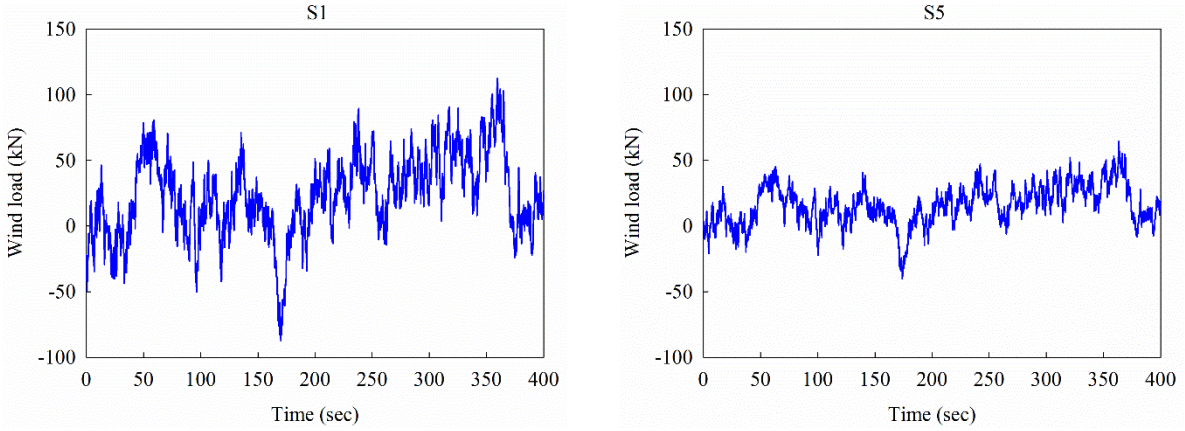

Fig. 9. Wind loads in segments S1 and S5

3.2. Wind load on the blades

The wind loads on the blades are influenced by the wind velocity, rotor velocity, pitch angle, the number of blades and geometrical configurations of the blade (e.g. blade profile, twist and chord distribution) [16]. To more realistically estimate the wind loads on the rotating blades, the blade element momentum (BEM) method, which couples the momentum theory with the local events taking place at the actual blades [9], is adopted in the present study. In the BEM method, it is assumed that all sections are independent along the rotor, i.e. no aerodynamic interaction between different sections. Each blade therefore can be divided into several elements and wind load on each element can be calculated separately [9].

The relative wind velocity on each element of the blade, v_{rel}, is given by

$$v_{rel}(r,t_s) = \sqrt{\left(\bar{v}(r,t_s)(1-a) + v_f(t_s)\right)^2 + \left(\Omega r(1+a')\right)^2} \tag{15}$$

where r is a radial distance of the element from the centre of the hub; t_s is time; a and a' are the axial and tangential induction factors respectively; Ω is the rotor velocity in rad/s; $\bar{v}$ is the mean wind velocity and v_f is the fluctuating wind velocity, the calculations of which are discussed below.

The height of each blade element $h(r,t_s)$ experiences a sinusoidal variation in magnitude as the rotation of the blades and the frequency of this variation is the same as the rotor frequency. With the definition of blade numbers in Fig. 2, $h(r,t_s)$ can be expressed as

$$h(r,t_s) = H_{hub} + r\cos(\Omega t_s + \theta_i) \tag{16}$$

$$\theta_i = \pi - \frac{2\pi}{3}(i-1) \quad i = 1,2,3 \tag{17}$$

where H_{hub} is the hub height and θ_i is the phase difference between blades. By submitting $h(r,t_s)$ into Eq. (10), the mean wind velocity $\bar{v}$ in Eq. (15) therefore can be obtained.

Due to the rotation of the blades, the PSD of the fluctuating wind velocity v_f is not a constant but varies with time, namely it is a time-variant rotational sampled spectrum. However, not to further complicate the problem, an isotropic, homogeneous turbulence at the hub height is assumed to represent the turbulence over the rotor field in the present study as suggested by many previous

studies (e.g. [16]). Based on this assumption, the fluctuating wind velocity v_f in Eq. (15) can be estimated by using the PSD of wind velocity at the hub height defined in Eq. (8).

After the relative wind velocity is determined (Eq. (15)), the local lift and drag forces on each element can be calculated as follows [9]

$$p_l(r,t_s) = \frac{1}{2}\rho v_{rel}^2(r,t_s) l(r) C_{lb}(\alpha) \tag{18}$$

$$p_d(r,t_s) = \frac{1}{2}\rho v_{rel}^2(r,t_s) l(r) C_{db}(\alpha) \tag{19}$$

in which, l is the chord length; C_{lb} and C_{db} are the lift and drag coefficients of the blade respectively and it is related to the local angle of attack, which is defined by

$$\alpha(r,t_s) = \varphi(r,t_s) - \beta(t_s) - \kappa(r) \tag{20}$$

where β is the pitch angle and it is 10° in the present study and κ is the pre-twist angle of each element with respect to the hub, which decreases from the bottom of 13.3° to the tip of 0° [1]. $\varphi(r,t_s)$ is the flow angle and it can be calculated as

$$\varphi(r,t_s) = \tan^{-1}\left(\frac{(1-a)\bar{v}(r,t_s) + v_f(t_s)}{(1+a')\Omega r}\right) \tag{21}$$

Fig. 10 shows the lift and drag coefficients of the blade with respect to the angle of attack.

The local wind loads in the directions parallel and perpendicular to the rotor plane therefore can be calculated by projecting the local lift and drag forces along the edgewise and flapwise directions respectively as shown in Fig. 11, which can be expressed as

$$\begin{Bmatrix} p_t(r,t_s) \\ p_n(r,t_s) \end{Bmatrix} = \begin{bmatrix} \sin(\varphi(r,t_s)) & -\cos(\varphi(r,t_s)) \\ \cos(\varphi(r,t_s)) & \sin(\varphi(r,t_s)) \end{bmatrix} \begin{Bmatrix} p_l(r,t_s) \\ p_d(r,t_s) \end{Bmatrix} \tag{22}$$

The total in-plane and out-of-plane wind loads on the blade then can be obtained by integrating the wind loads on each blade element over the entire rotor length as

$$F_t(t_s) = \int_0^R p_t(r,t_s)\phi_{e,1}(r)dr \tag{23}$$

$$F_n(t_s) = \int_0^R p_n(r,t_s)\phi_{f,1}(r)dr \tag{24}$$

where R is rotor radius, $\phi_{e,1}$ and $\phi_{f,1}$ are the fundamental vibration mode shapes of the blade in the edgewise and flapwise directions respectively, which are obtained by carrying out an eigenvalue analysis and they are shown in Fig. 12.

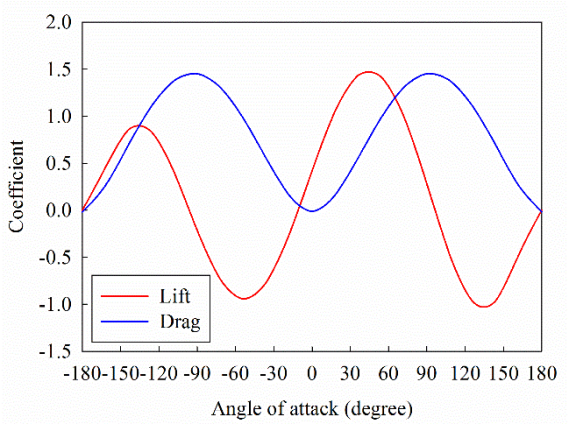

Fig. 10. Lift and drag coefficients of the blade

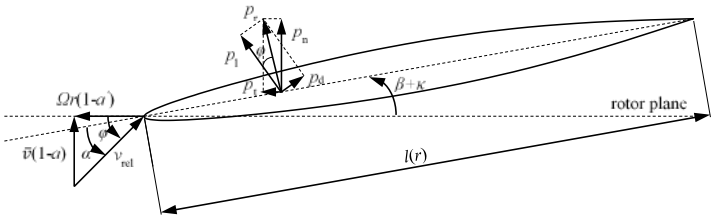

Fig. 11. Wind loads on the blade element

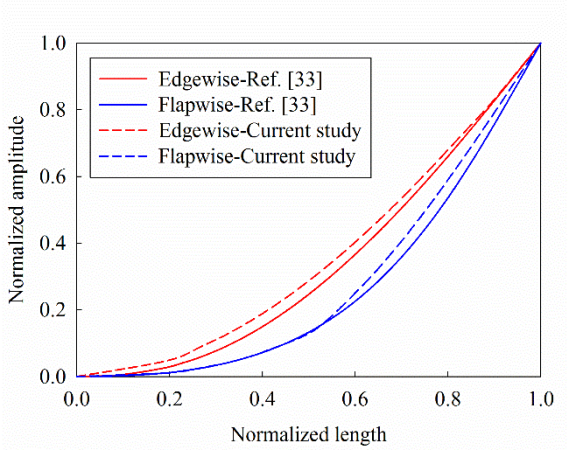

Fig. 12. First edgewise and flapwise vibration mode shapes of the blade

Based on the BEM method discussed above, the total in-plane and out-of-plane wind loads of a rotating blade can be calculated. When the parked condition is of interest, the same procedure can be followed, and the above equations can be simplified by submitting Ω=0 into Eqs. (15), (16), and (21).

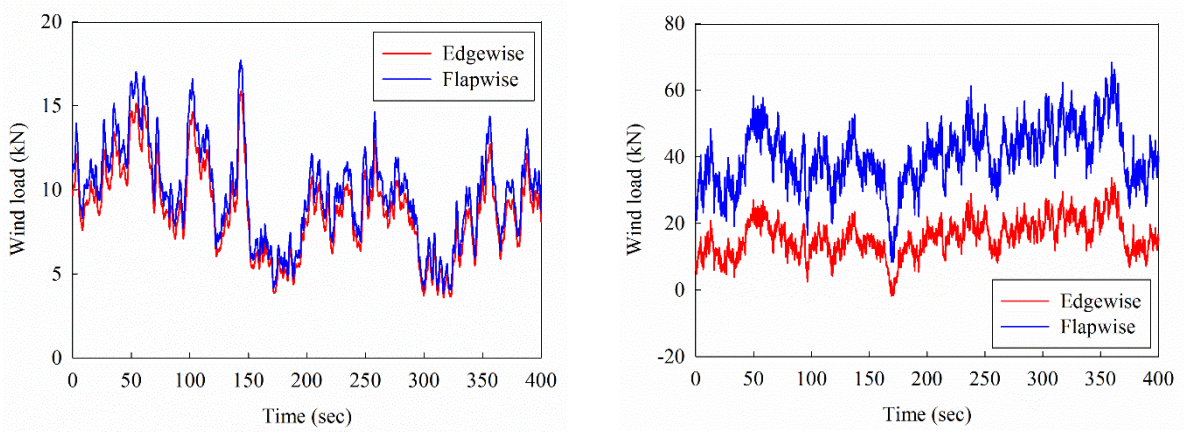

(a) Parked condition (b) Operating condition

Fig. 13. Edgewise and flapwise wind loads on Blade 2

The wind loads on each blade of the wind turbine when it is in the parked and operating conditions therefore can be simulated and Fig. 13 shows the edgewise and flapwise wind loads on Blade 2 under different conditions. In this simulation, the mean wind velocity at the tower top is 15 m/s and the rotor speed is 12.1 rounds per minute. For conciseness, the wind loads on other two blades are not shown. As shown in Fig. 13(a), the flapwise wind loads are slightly larger than the edgewise wind loads when the wind turbine is in the parked condition, this is because the flow angle is a constant and equals to $\pi/2$ based on Eq. (21) when Ω=0 and the angle of attack is between 67 and 80 degrees, therefore the lift and drag coefficients have a small difference as shown in Fig. 10, which in turn lead to non-significant difference between the flapwise and edgewise wind loads on the parked blades. When the wind turbine is in the operating condition, the wind loads in the edgewise and flapwise directions are obviously different and the wind load in the flapwsie direction is larger than that in the edgewise direction. Moreover, comparing Fig. 13(a) with 13(b), it is obvious that the wind loads on the rotating blades are much larger than those on the parked blades since the relative wind velocity becomes larger based on Eq. (15) due to the rotation of the blades.

3.3. Sea wave load on the monopile

To calculate the sea wave load acting on the monopile, the JONSWAP spectrum, which has the following form [45] is used to simulate the sea surface elevation

$$S_{\eta\eta}(f) = \alpha_P g^2 (2\pi)^{-4} f^{-5} exp\left[-\frac{5}{4}\left(\frac{f_m}{f}\right)^4\right] \gamma^{exp\left[-\frac{(f-f_m)^2}{2\sigma^2 f_m^2}\right]} \quad (25)$$

where η is the sea surface elevation; g is the gravitational acceleration; γ is the peak enhancement factor (typically 3.3 [4]) and f is frequency in Hz. α_P, f_m and σ are three constants, which are [4]

$$\alpha_P = 0.076(Fg/v_{10}^2)^{-0.22} \quad (26)$$

$$f_m = 11(v_{10}F/g^2)^{-1/3}/\pi \quad (27)$$

and

$$\sigma = \begin{cases} 0.07 & f \le f_m \\ 0.09 & f > f_m \end{cases} \quad (28)$$

in which v_{10} is the mean wind velocity at 10 m above sea surface and F is the fetch length.

The sea surface elevation $\eta(t_s)$ in the time domain then can be simulated as

$$\eta(t_s) = \sum_{i=1}^{n} \sqrt{2d\omega S_{\eta\eta}(\omega_i)} \cos\left(\omega_i t_s + \Phi(\omega_i)\right) \quad (29)$$

where Φ is the random phase angle uniformly distributed over the range of [0, 2π].

The velocity and acceleration of water particles in the horizontal direction can be expressed as [46]

$$v_x = \frac{H\omega}{2} \frac{\cosh k_w(d_w + z_w)}{\sinh k_w d_w} \cos(k_w x_w - \omega t_s + \varphi) \quad (30)$$

$$a_x = \frac{H\omega^2}{2} \frac{\cosh k_w(d_w + z_w)}{\sinh k_w d_w} \sin(k_w x_w - \omega t_s + \varphi) \quad (31)$$

in which x_w and z_w denote the horizontal and vertical coordinates respectively; d_w is water depth, which is 20 m in the present study; H is the wave height, which is two times of the amplitude of the sea surface elevation; ω is angular frequency in rad/s and k_w is the sea wave number, which can be estimated based on the following equation [46]

$$\omega^2 = g k_w \tanh(k_w d_w) \quad (32)$$

In the present study, the following parameters are used: g=9.8 m/s^2, v_{10}=11.5 m/s and F=40,000 m. The peak wave frequency f_m is therefore 0.208 Hz based on Eq. (27) and the wave period is T=1/f_m=

4.81 s. The wave length can be calculated as $\lambda=gT^2/2\pi=36$ m [46], and it is larger than five times of the diameter of the monopile. Based on the specifications in [32], the Morison formula can be used to calculate the sea wave load. According to the Morison equation, the transverse sea wave load per unit length of the monopile can be calculated as

$$F_w = \frac{1}{2}\rho_w C_{dp} d_p |v_x| v_x + \rho_w C_m A_p a_x \tag{33}$$

$$C_m = C_a + 1 \tag{34}$$

where C_{dp}, C_m are the drag and inertia coefficients respectively, and C_{dp}=1.2, C_m=2.0 are adopted in the simulation. It should be noted that the first term represents the contribution of the quadratic drag force, and the second term is the inertia force.

In the simulation, the monopile in the water is divided into two segments and the length of each segment is 10 m. Fig. 14 shows the PSDs of the simulated sea surface elevation and the given model, good match is observed. Fig. 15 shows the simulated sea wave load time history at the mean sea level; the sea wave loads at other locations along the monopile are not shown for conciseness.

As mentioned above, the blade, tower and monopile in the sea water are divided into a few segments. In the FE model, a reference point is defined in each segment and coupled with the cross section of the corresponding segment, the simulated wind and sea wave loadings are applied on these reference points.

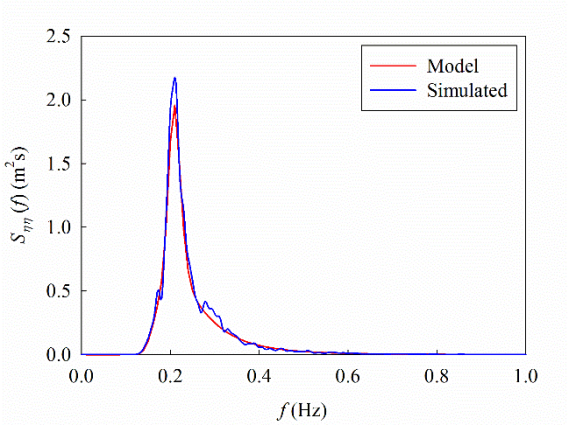

Fig. 14. Comparison between the simulated sea surface elevation and the model PSDs

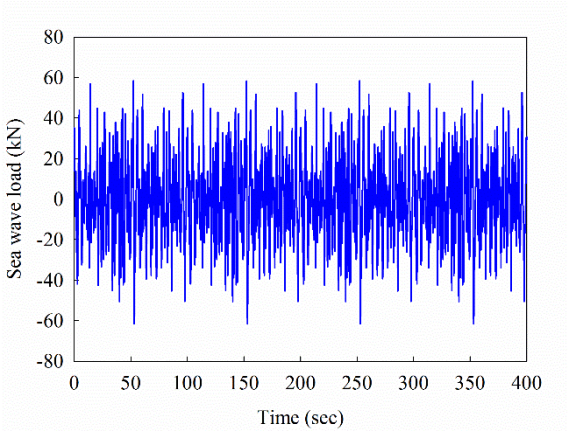

Fig. 15. Sea wave load time history at mean sea level

4. Numerical results

4.1. Influence of operational conditions

To examine the influence of operational conditions of wind turbine on the structural responses, two cases are investigated in this section. In the first case, the wind turbine is in the parked condition, with the locations of the blades shown in Fig. 2(a). In the second case, the blades are rotating with a uniform angular velocity of Ω=1.27 rad/s, which corresponds to the rated rotor speed of NREL 5 MW wind turbine (12.1 rpm). The wind and sea wave loads shown in Figs. 9 and 15 are applied to the tower respectively in both cases. For the wind loads on the blades, they depend on the rotor velocity as discussed in Section 3.2. Different wind loads as shown in Fig. 13 are applied in different cases. In both cases, a duration of 400 s is considered for all the external vibration sources. Not to further complicate the problem, SSI is not considered in this section, i.e. the wind turbine is fixed at the sea bed level.

It is obvious that the responses along the tower are different and the maximum responses occur at the tower top. For conciseness, only the maximum responses are discussed in the present study. Fig. 16 shows the displacement time histories at the top of the tower in the fore-aft and side-to-side directions. The red curves are the results when the blades are in the parked condition, and the blue curves are the displacements when they are rotating. It shows that the displacements in the operating condition are larger than those in the parked condition in both directions. As shown in Fig. 16(a), the maximum fore-aft displacement at the top of the tower is 0.473 m occurring at t=171 s when the wind turbine is

still. When the blades are rotating, a larger maximum displacement of 0.674 m occurs at t=362 s. For the side-to-side displacement at the top of the tower, the maximum values are 0.093 and 0.206 m respectively when the wind turbine is in the parked and operating conditions (Fig. 16(b)). These results are actually expected since as shown in Fig. 13, when the blades are rotating, the wind loads acting on the blades are larger compared to the parked condition. Larger wind loads on the blades result in more severe interaction between the tower and blades and therefore larger tower responses. These results indicate that previous studies by assuming the wind turbines in the parked condition may result in non-conservative structural response estimations, which in turn may lead to the unsafe design of structural components.

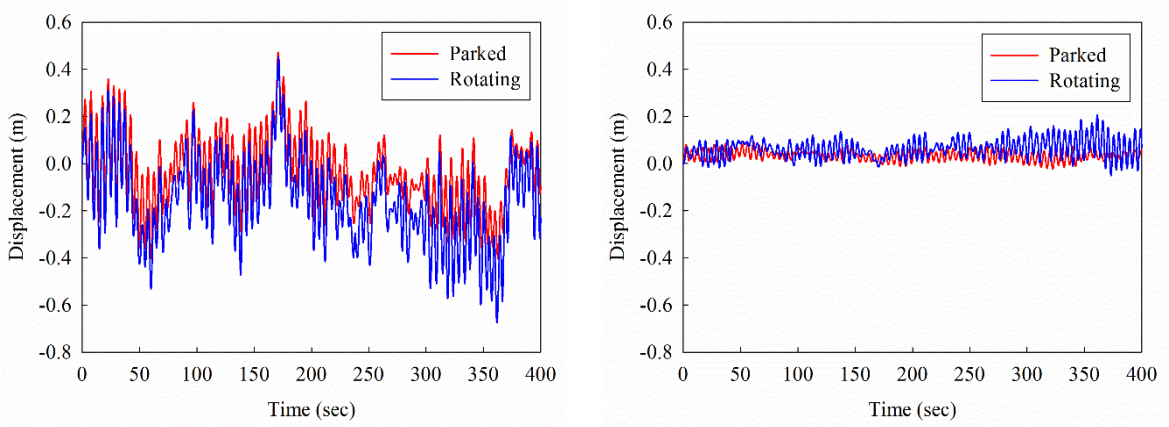

(a) Fore-aft (b) Side-to-side

Fig. 16. Fore-aft and side-to-side displacement time histories at the tower top

Comparing Fig. 16(a) with 16(b), it is obvious that the side-to-side displacements of the tower are much smaller than the fore-aft responses in both cases. Two reasons lead to these results. The first one is that the wind and sea wave loads are only applied in the fore-aft direction on the tower in the numerical simulation, and no external vibration sources are acted in the side-to-side direction. The other reason is that as shown in Fig. 13, the wind loads on the blades in the flapwise (fore-aft direction corresponds to tower) and edgewise (side-to-side) directions are almost the same when the wind turbine is in the parked condition (Fig. 13(a)), while when it is in the operating condition, the wind loads in the flapwise direction are much larger than those in the edgewise direction (Fig. 13(b)). The

497 larger wind loads on the blades result in more severe interaction between the tower and blades, and
498 lead to the larger tower responses in the fore-aft direction as discussed above.
499 Fig. 17 shows the PSDs of the acceleration responses at the top of the tower in the fore-aft and side-
500 to-side directions when the blades are in the parked and operating conditions. To more clearly obtain
501 the dominant frequencies of the structural responses, an N/4-point Hamming window is used to
502 smooth the PSDs in the present study, in which N is the number of the data to be analysed. As shown
503 in Fig. 17(a), an obvious peak appears at 0.204 Hz. As shown in Table 5 in Section 4.2, this value
504 corresponds to the first vibration mode of the tower in the fore-aft direction, which means the first
505 vibration mode is excited by the external vibration sources. Fig. 17 also shows that another peak
506 occurs at 0.603 and 0.647 Hz respectively when the wind turbine is in the parked and operating
507 conditions. As shown in Table 5, 0.603 Hz is the first collective flap vibration mode of the blades
508 when the wind turbine is in the parked condition. For 0.647 Hz, this frequency cannot be directly
509 found in Table 5, this is because the rotating condition cannot be directly considered in the modal
510 analysis by using ABAQUS. This frequency corresponds to the first collective flap vibration mode of
511 the blades when the wind turbine is in the operating condition. These results indicate again that the
512 interaction between the tower and blades makes the vibrations of the blades contribute to the tower
513 responses. Compared to the parked condition, the first collective flap vibration frequency of the
514 blades is slightly larger when it is in the operating condition as shown in Fig. 17(a). This is because
515 the centrifugal stiffness of the blades is generated when the wind turbine is operating, which in turn
516 leads to large structural stiffness and vibration frequency of the blades. For the PSDs in the side-to-
517 side direction, Fig. 17(b) shows that only one peak appears at 0.208 Hz, and this peak corresponds to
518 the first vibration mode of the tower in the side-to-side direction as shown in Table 5. Comparing the
519 results in Fig. 17(b) with those in Fig. 17(a), it is obvious that the energies are much smaller in the
520 side-to-side direction, which results in the smaller tower responses in this direction as shown in Fig.
521 16. Similarly, compared to the red curve, the values in the blue curve are larger, and this explains the
522 larger structural responses in the operating condition as shown in Fig. 16.
523

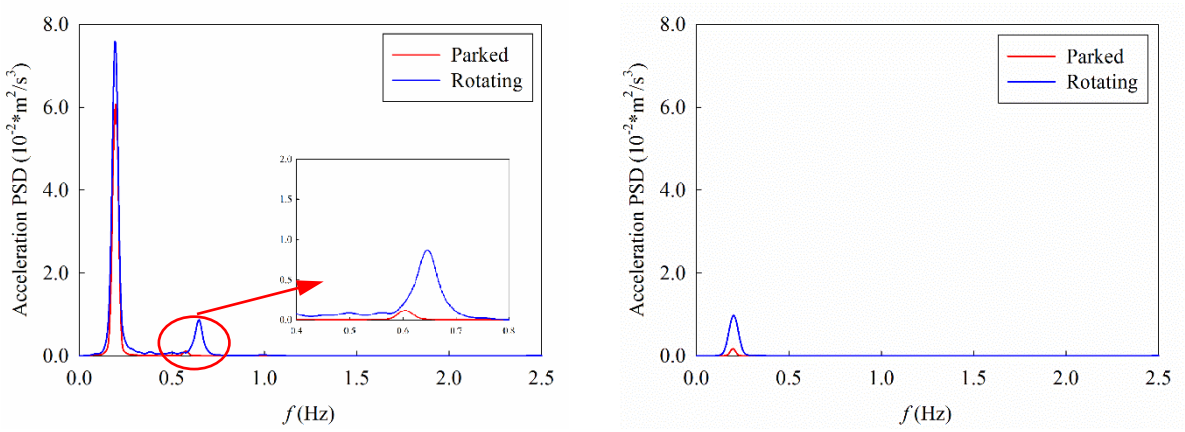

(a) Fore-aft (b) Side-to-side

Fig. 17. Fore-aft and side-to-side acceleration PSDs at the tower top

Fig. 18 shows the displacement (relative to the tower top) time histories at the tips of blades in the flapwise direction. Wind load acting on the blade can be decomposed into a constant mean and a fluctuating component as discussed in Section 3. The mean value of the fluctuating term is zero. However, the total wind load on the blade has a non-zero mean because of the constant component of the wind pressure as shown in Fig. 13, which results in the non-zero baseline of the structural responses shown in Fig. 18. As shown, the maximum flapwise displacements at the tips of Blades 1, 2 and 3 are 0.429, 0.544, 0.544 m respectively when the wind turbine is in the parked condition. The displacements at the tips of Blades 2 and 3 are the same. This is because the geometrical configurations and locations of Blades 2 and 3 are the same as shown in Fig. 2 and the same excitations are applied on these two blades, which in turn lead to the same structural responses. The result also shows that the maximum flapwise displacement on Blade 1 is smaller than that on Blades 2 and 3, this is because Blade 1 is lower than Blades 2 and 3 (see Fig. 2), and the wind loads on Blade 1 are smaller than those on Blades 2 and 3. Fig. 18 also shows that the maximum displacements are much larger when the blades are rotating and the corresponding values are 1.074, 1.338, 1.274 m respectively. When the wind turbine is in the operating condition, the flapwise vibrations of the blades are not the same and they are influenced by the original locations of the blades.

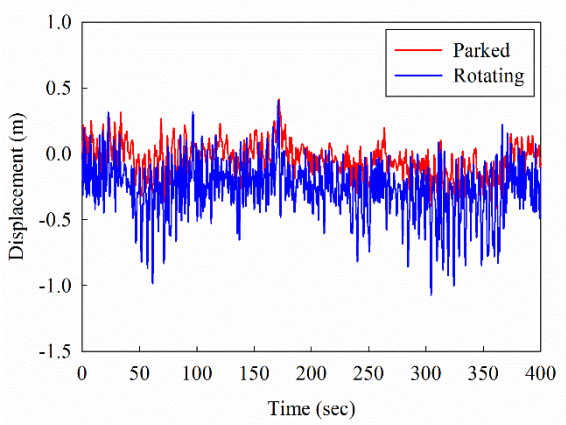

(a) Blade 1

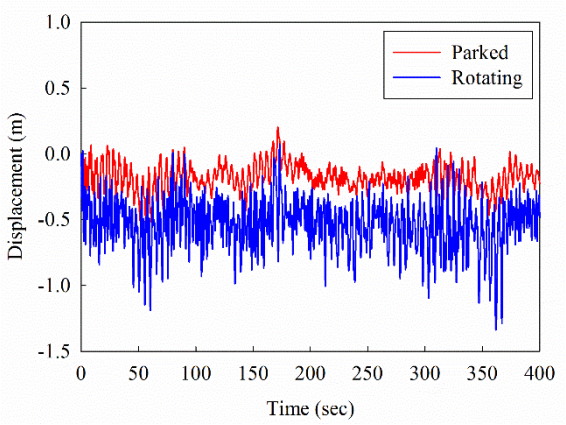

(b) Blade 2

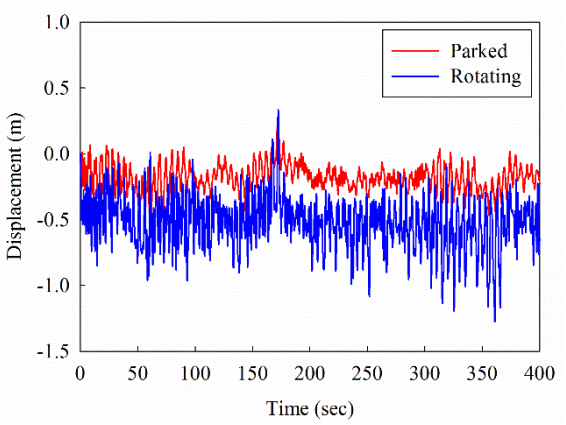

(c) Blade 3

543 Fig. 18. Flapwise displacement time histories at the blade tips

544

545 Fig. 19 shows the edgewise displacements of the blades when they are in the parked and operating
546 conditions. Again, the non-zero baseline of the edgewise displacements is due to the contribution of
547 the mean term of the wind loads acting on the blades. As shown in Fig. 19(a), the maximum edgewise
548 displacements at the tips of Blades 1, 2 and 3 are 0.067, 0.138 and 0.138 m respectively when the
549 turbine is in the parked condition. When the blades are rotating, as shown in Fig. 19(b), the edgewise
550 responses of the three blades are identical because of the same geometrical and structural parameters
551 in the rotor plane. Compared to the parked condition, the edgewise displacements of the blades are
552 much larger when they are rotating. The edgewise displacements at the tips of the blades experience a
553 sinusoidal variation in magnitude after about 25 s and the frequency of this variation equals to the
554 rotor frequency of 0.202 Hz (1.27 rad/s). At the first 25 s, the amplitudes of the edgewise

displacements are larger than those after 25 s since the blades rotate immediately from the parked state at t=0 s and the whole wind turbine system is unstable during this period [47]. Due to the structural and aerodynamic damping of the blades, the displacements decrease to an almost constant value from t=25 s. These results are consistent with those reported in [33, 47].

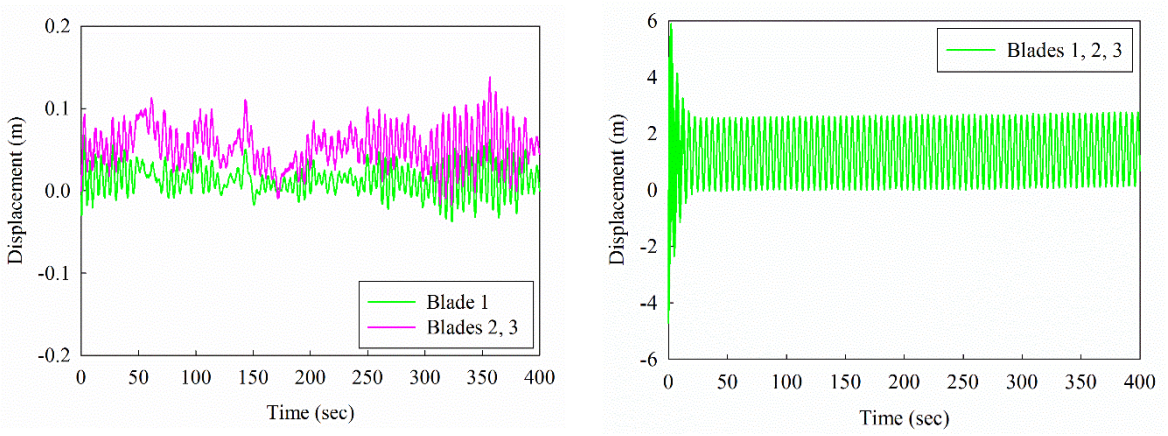

(a) Parked (b) Rotating

Fig. 19. Edgewise displacement time histories at the blade tips

To further explain the above results, Fig. 20 shows the PSDs of the acceleration responses at the tip of Blade 2 in the flapwise and edgewise directions respectively. The acceleration PSDs of other blades are similar with those of Blade 2, they are therefore not shown for brevity. As shown in Fig. 20(a), three obvious peaks appear at 0.204, 0.544 and 0.603 Hz respectively when the wind turbine is in the parked condition. The first peak corresponds to the first fore-aft vibration mode of the tower, because of the interaction between the tower and blades as discussed above. Another two peaks correspond to the first flapwise pitch and collective flap vibration modes of the blades as shown in Table 5 in Section 4.2. It should be noted that the first flapwise yaw vibration mode of the blades is not excited since the locations of the blades and wind loads acting on the blades are symmetric and the flapwise yaw vibration mode is antisymmetric as shown in Fig. 6. The antisymmetric vibration mode cannot be excited by the symmetric load when it is acting on a symmetric structure. When the blades are rotating, the three peaks occur at 0.204, 0.565 and 0.647 Hz respectively. Again the last two vibration frequencies cannot be obtained from Table 5 due to the blades rotation cannot be directly considered

in the modal analysis as discussed above. For the PSDs in the edgewise direction, Fig. 20(b) shows that two peaks appear at 0.208 and 1.176 Hz respectively when the wind turbine is in the parked condition and these two peaks correspond to the first vibration modes of the tower and blades in the edgewise direction (side-to-side direction for the tower) as shown in Table 5. However, when the wind turbine is operating, only one peak occurs at the rotor frequency of the blades (0.202 Hz). This result well explains that the edgewise displacements of the rotating blades are governed by the rotor rotation as shown in Fig. 19(b). Fig. 20 also clearly shows the operating condition of wind turbine leads to larger responses of the blades as shown in Figs. 18 and 19 in both the flapwise and edgewise directions.

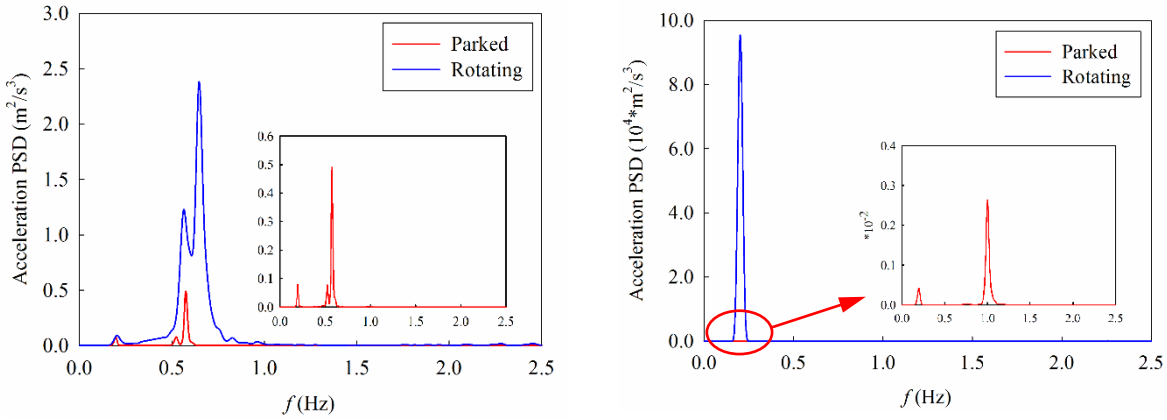

(a) Flapwise (b) Edgewise

Fig. 20. Flapwise and edgewise acceleration PSDs at the tip of Blade 2

4.2. Influence of SSI

To investigate the effect of SSI on the dynamic behaviours of the wind turbine, three different soils with undrained shear strength of s_u=25, 50 and 100 kPa are considered in the present study and are used to represent the typical soft, medium and stiff soils. As discussed above, the rotation of the blades cannot be explicitly considered in the modal analysis by using ABAQUS, only the parked condition is considered when the vibration characteristics (vibration frequencies and vibration modes) of the wind turbine are calculated. Table 5 tabulates the vibration frequencies of the wind turbine without and with the consideration of SSI. The corresponding differences between the vibration

595 frequencies obtained without and with SSI are also given in the table. As shown in Table 5, SSI can
596 significantly decrease the vibration frequencies of the tower especially for the soft soil condition, this
597 is because the monopile inserts into the sea bed and is surrounded by the soil when SSI is considered,
598 which makes the tower more flexible compared to the case of the wind turbine fully fixed at the sea
599 bed level. Since the stiffness of the tower becomes smaller, the vibration frequencies of the tower
600 therefore decrease. For example, when the undrained shear strength of the soil s_u is 25 kPa, the first
601 vibration frequency of the tower in the fore-aft direction is 0.141 Hz, and it is 0.204 Hz when SSI is
602 not considered. The reduction ratio reaches 30.9%. It should be noted that the energy of the wind load
603 concentrates within the range of 0-0.1 Hz as shown in Fig. 7, when SSI is considered, the first
604 vibration frequency of the tower is closer to the dominant frequency of the wind load. In this case,
605 resonance might occur and larger structural responses are expected. Therefore, SSI should be
606 considered to more accurately predict the dynamic responses of the wind turbine.
607
608 **Table 5**
609 Vibration frequencies of the wind turbine without and with SSI

Mode	Description	w/o SSI	s_u=25 kPa		s_u=50 kPa		s_u=100 kPa	
		(Hz)	Frequency (Hz)	Difference (%)	Frequency (Hz)	Difference (%)	Frequency (Hz)	Difference (%)
1	tower fore-aft (1st order)	0.204	0.141	-30.9	0.154	-24.5	0.163	-20.1
2	tower side-to-side (1st order)	0.208	0.142	-31.7	0.156	-25.0	0.165	-20.7
3	blade flapwise yaw (1st order)	0.488	0.474	-2.9	0.474	-2.9	0.474	-2.9
4	blade flapwise pitch (1st order)	0.544	0.532	-2.2	0.536	-1.5	0.538	-1.1
5	blade collective flap (1st order)	0.603	0.594	-1.5	0.596	-1.2	0.598	-0.8
6	blade edgewise pitch (1st order)	1.176	1.189	1.1	1.206	2.6	1.145	-2.6
7	blade edgewise yaw (1st order)	1.206	1.231	2.1	1.250	3.6	1.154	-4.3
8	tower fore-aft (2nd order)	1.562	1.036	-33.7	1.121	-28.2	1.242	-20.5
9	tower side-to-side (2nd order)	1.630	1.003	-38.5	1.096	-32.8	1.279	-21.5
10	blade flapwise yaw (2nd order)	1.700	1.625	-4.4	1.626	-4.4	1.626	-4.4

610

Different from modal analysis, the wind turbine is assumed in the operating condition when the structural responses are calculated. In this section, a rotor angular velocity of Ω=1.27 rad/s is considered.

Fig. 21 shows the displacement time histories at the top of the tower in the fore-aft and side-to-side directions without and with the consideration of SSI. Table 6 tabulates the maximum fore-aft and side-to-side displacements at the tower top, and the corresponding differences between the peak displacements without and with SSI are given in the table as well. As shown in Fig. 21, the tower vibrations are much larger in both the fore-aft and side-to-side directions when SSI is considered, and with the increment of soil shear strength, the lateral stiffness of soil increases and the deflection of monopile decreases [36]. As shown in Fig. 21(a) and Table 6, the maximum fore-aft displacements at the top of the tower are 1.742, 1.383 and 1.297 m respectively when s_u=25, 50 and 100 kPa, which increase by 158.5%, 105.2% and 92.4% respectively compared to that when the wind turbine is fixed at the sea bed level, i.e. neglecting the interaction between the monopile foundation and the surrounding soil. Fig. 21(b) and Table 6 also show that the peak displacements at the tower top in the side-to-side direction are 0.388, 0.301 and 0.269 m respectively. Compared to the case in which SSI is not considered, these values are increased by 88.3%, 46.1% and 30.6%.

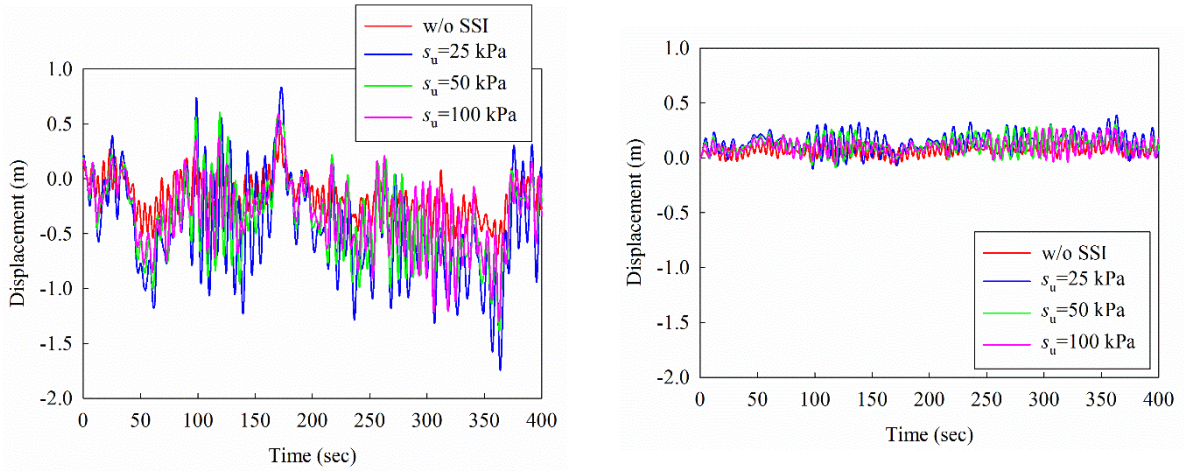

(a) Fore-aft (b) Side-to-side

Fig. 21. Fore-aft and side-to-side displacement time histories at the tower top without and with SSI

Table 6

Maximum displacements at the tower top without and with SSI

Direction	w/o SSI (m)	s_u=25 kPa Displacement (m)	s_u=25 kPa Difference (%)	s_u=50 kPa Displacement (m)	s_u=50 kPa Difference (%)	s_u=100 kPa Displacement (m)	s_u=100 kPa Difference (%)
Fore-aft	0.674	1.742	158.5	1.383	105.2	1.297	92.4
Side-to-side	0.206	0.388	88.3	0.301	46.1	0.269	30.6

Fig. 22 shows the PSDs of the acceleration responses at the top of the tower in the fore-aft and side-to-side directions without and with the effect of SSI. As shown in Fig. 22(a), the first vibration frequency of the tower in the fore-aft direction shifts to a lower value when SSI is considered, and they are 0.141, 0.154 and 0.163 Hz respectively when s_u=25, 50 and 100 kPa. It should be noted that the second peak appearing at 0.647 Hz corresponds to the first collective flap vibration mode of the blades and this frequency is almost not influenced by SSI as shown in Fig. 22, which well agrees with the observations in Table 5 that SSI has almost no effect on the vibration frequencies of the blades. Similarly, as shown in Fig. 22(b), the first vibration frequency of the tower in the side-to-side direction decreases as well when the effect of SSI is included. The corresponding vibration frequencies are 0.142, 0.156 and 0.165 Hz respectively when s_u=25, 50 and 100 kPa. Fig. 22 also shows that more energies are obtained for the softer soil, which in turn result in the larger tower responses as shown in Fig. 21.

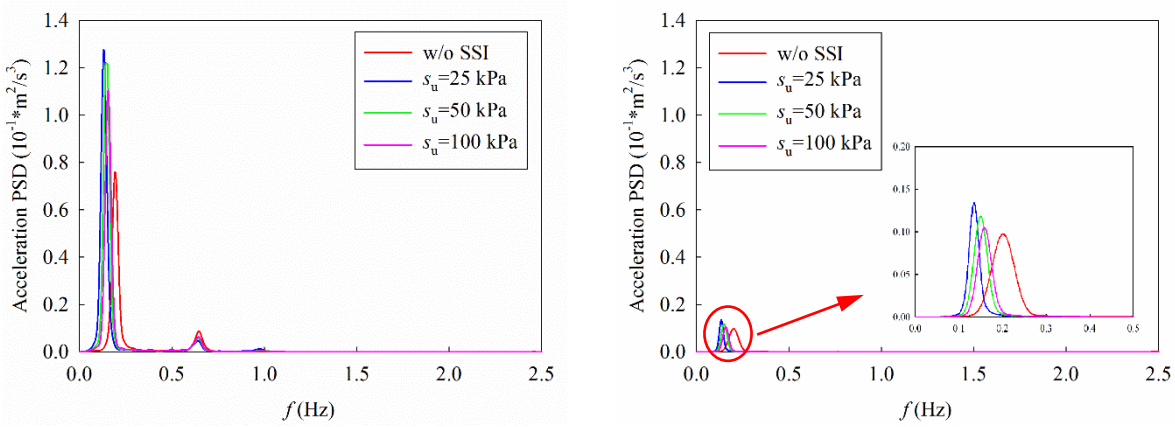

(a) Fore-aft (b) Side-to-side

Fig. 22. Fore-aft and side-to-side acceleration PSDs at the tower top without and with SSI

Fig. 23 shows the displacement time histories at the tips of the blades in the flapwise direction. Table 7 tabulates the maximum flapwise displacements at each blade tip and the corresponding differences when SSI is considered or not. As shown in Table 7, the largest displacements at the tip of Blade 1 are 1.536, 1.231 and 1.220 m respectively when s_u=25, 50 and 100 kPa. For Blade 2, the maximum values are 1.745, 1.648 and 1.632 m respectively, and the corresponding values are 1.701, 1.529 and 1.486 m respectively for Blade 3. It can be seen that the flapwise displacement responses of the blades are influenced by SSI but the extents are smaller than those of the tower (refer to Table 6). This is because the soil springs are directly connected to the monopile foundation of the tower while the influence of SSI on the blades is mainly through the (indirect) interaction between the tower and blades. As discussed above, softer soil leads to larger fore-aft vibrations of the tower, which in turn leads to the more severe interaction between the tower and blades, and therefore the larger flapwise displacements of the blades.

Fig. 24 shows the edgewise displacement time histories at the tip of Blade 2, and the displacements at other two blades are not shown since they are the same as discussed above. As shown, again the edgewise displacements of the rotating blades are governed by the rotor rotation and SSI has a negligible effect on the displacement responses of the blades in the edgewise direction. This is because the vibrations of the tower in the side-to-side direction are very small as shown in Fig. 21(b), which results in the negligible interactions between the tower and blades in the side-to-side direction. The results are consistent with those reported by Fitzgerald and Basu [17].

Fig. 25 shows the PSDs of the acceleration responses at the tip of Blade 2 in the flapwise and edgewise directions. As shown in Fig. 25(a), three obvious peaks appear in the PSD curves and they correspond to the first fore-aft vibration mode of the tower, the first flapwise pitch and collective flap vibration modes of the blades respectively as discussed in Section 4.1. As shown, the frequency corresponding to the first peak changes when SSI is considered and the value becomes smaller when softer soil is considered. This is easy to understand, when softer soil is considered, the system becomes more flexible. For the second and third peaks, they correspond to the vibration modes of the blades and they are almost not influenced by SSI. Fig. 25(b) shows that only one peak occurs at the rotor frequency of the blades (0.202 Hz) and the energies included in the PSD curves are the same

when s_u=25, 50 and 100 kPa. This result again explains the results that SSI has no effect on the edgewise responses of the blades as shown in Fig. 24.

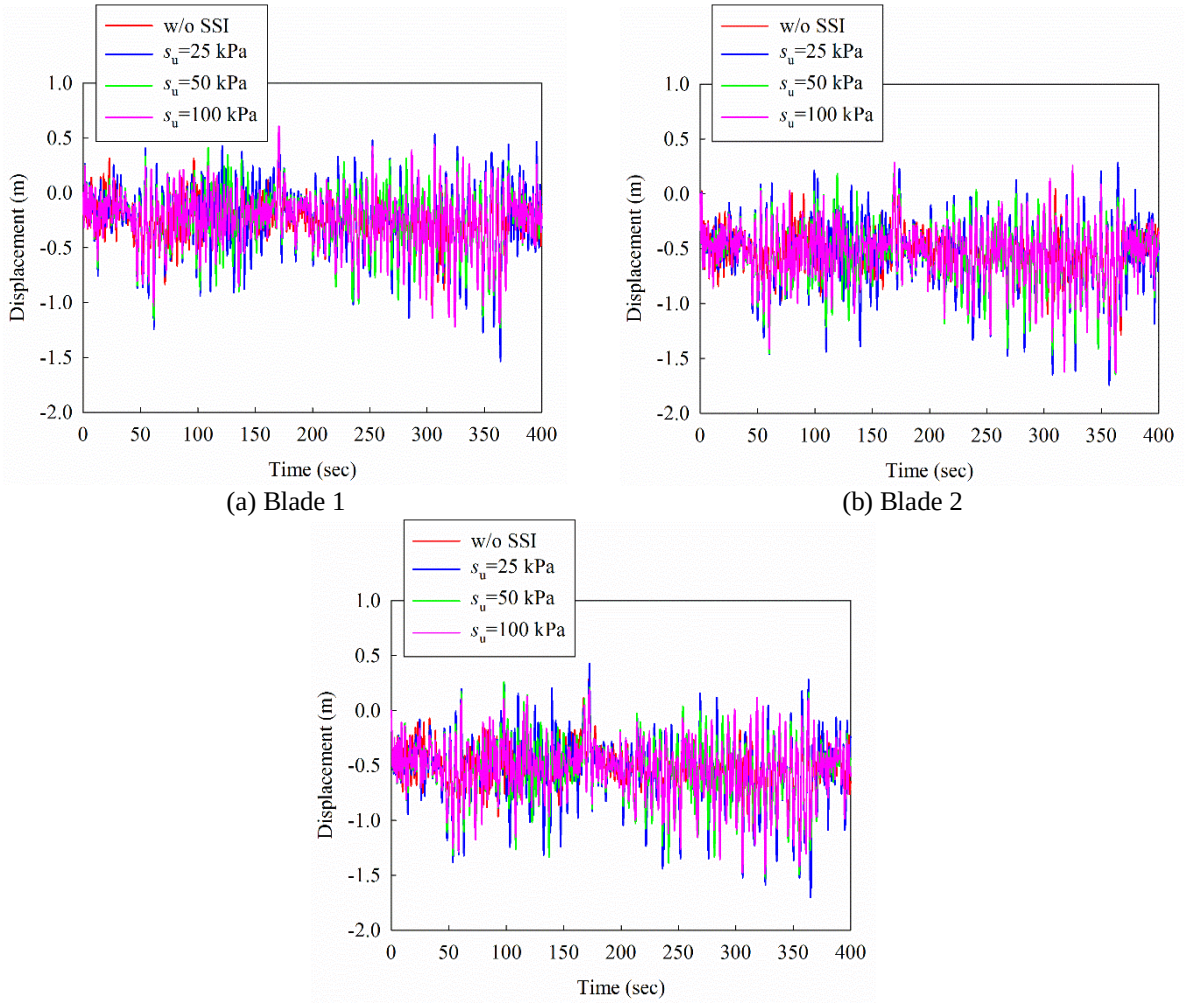

(a) Blade 1 (b) Blade 2

(c) Blade 3

Fig. 23. Flapwise displacement time histories at the blade tips without and with SSI

Table 7

Maximum flapwise displacements at the blade tip without and with SSI

Location	w/o SSI (m)	s_u=25 kPa Displacement (m)	s_u=25 kPa Difference (%)	s_u=50 kPa Displacement (m)	s_u=50 kPa Difference (%)	s_u=100 kPa Displacement (m)	s_u=100 kPa Difference (%)
Tip of Blade 1	1.074	1.536	43.0	1.231	14.6	1.220	13.6
Tip of Blade 2	1.338	1.745	30.4	1.648	23.2	1.632	22.0
Tip of Blade 3	1.274	1.701	33.5	1.529	20.0	1.486	16.6

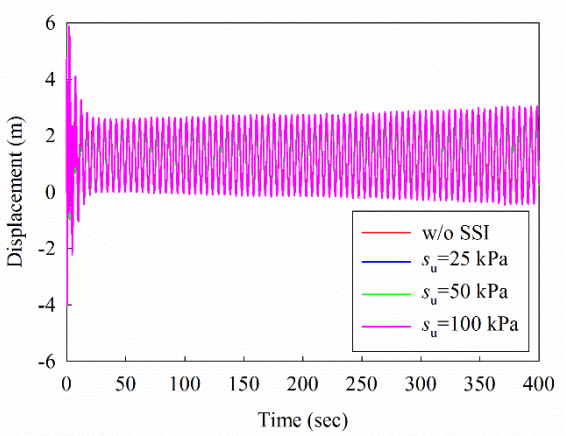

Fig. 24. Edgewise displacement time histories at the tip of Blade 2 without and with SSI

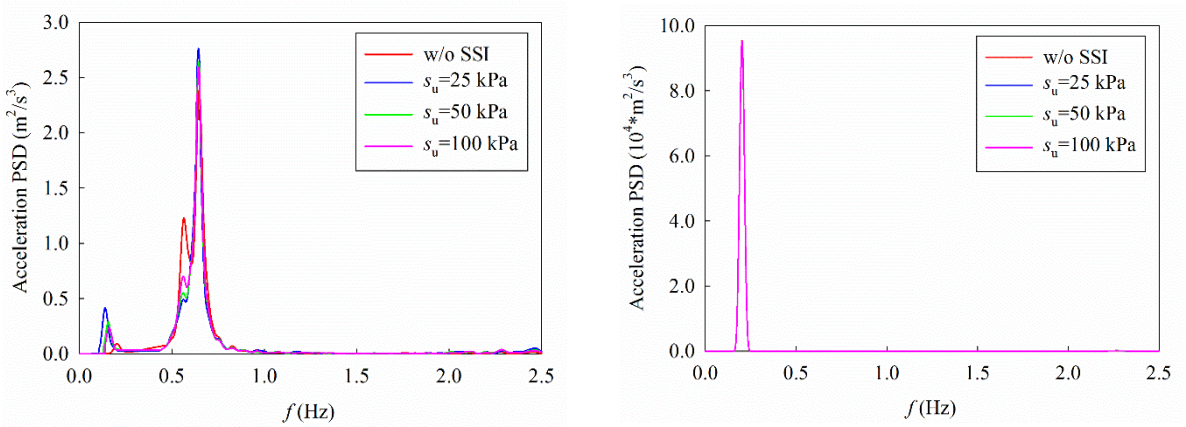

(a) Flapwise (b) Edgewise

Fig. 25. Flapwise and edgewise acceleration PSDs at the tip of Blade 2 without and with SSI

4.3. Influence of rotor velocity

The rotor velocity may also significantly influence the structural responses. The designed cut-in and rated rotor velocities of the NREL 5 MW wind turbine are 6.9 and 12.1 rpm respectively as tabulated in Table 1. In other words, the wind turbine starts to rotate at a (cut-in) rotor speed of 6.9 rpm and the maximum energy output of the wind turbine will be achieved at a (rated) rotor speed of 12.1 rpm. To examine the influence of rotor velocity, the rotor velocity of 8 rpm (0.84 rad/s) and 12.1 rpm (1.27 rad/s) are investigated, which are within the designed rotor velocity range. Another rotor velocity of 16 rpm (1.68 rad/s) is also considered to represent a worst rotating condition in the present study. SSI is also considered in this section and the undrained shear strength of soil is taken as 50 kPa.

As discussed in Section 3.2, the wind loads on the blades are influenced by the rotor velocity. Fig. 26 shows the simulated wind loads on Blade 2 in the flapwsie and edgewise directions when the rotor velocities are 0.84 and 1.68 rad/s respectively. Together with the wind loads shown in Fig. 13(b) (the wind loads when Ω=1.27 rad/s), it can be seen that larger rotor velocity results in larger wind loads acting on the blade. For conciseness, the wind loads acting on the other two blades are not plotted in the figure. Similar trend is obtained.

Fig. 27 shows the displacement time histories at the top of the tower in the fore-aft and side-to-side directions and the maximum displacements are tabulated in Table 8. As shown in Fig. 27 and Table 8, the displacement responses at the top of the tower are increased in both directions with the increment of rotor velocity. The maximum fore-aft displacements at the tower top are 1.226, 1.383 and 1.523 m respectively when Ω=0.84, 1.27 and 1.68 rad/s, and the corresponding values in the side-to-side direction are 0.258, 0.301 and 0.329 m. This is because wind loads acting on the blades are larger with the increment of the rotor velocity as discussed above, and larger loads result in larger structural responses.

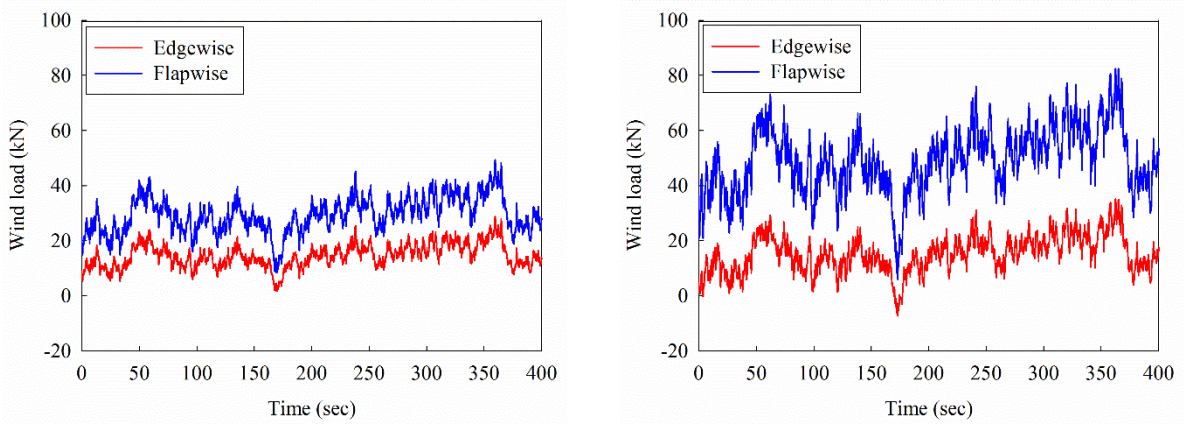

(a) Ω=0.84 rad/s (b) Ω=1.68 rad/s

Fig. 26. Wind loads on Blade 2 under different rotor velocities

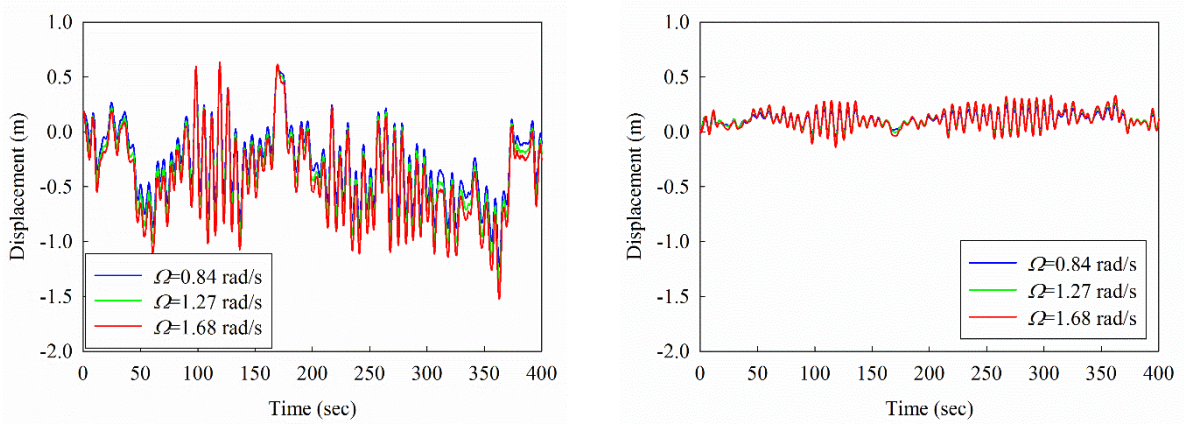

(a) Fore-aft (b) Side-to-side

713 Fig. 27. Fore-aft and side-to-side displacement time histories at the tower top under different rotor velocities

714

715 **Table 8**

716 Maximum displacements at the tower top under different rotor velocities (Unit: m)

Direction	Ω=0.84 rad/s	Ω=1.27 rad/s	Ω=1.68 rad/s
Fore-aft	1.226	1.383	1.523
Side-to-side	0.258	0.301	0.329

717

718 Fig. 28 shows the PSDs of the fore-aft and side-to-side acceleration responses at the top of the tower.
719 As shown in Fig. 28(a), the first peak appears at 0.154 Hz, which corresponds to the first fore-aft
720 vibration frequency of the tower and is not influenced by the rotor velocity. The second peak
721 corresponds to the first collective flap vibration mode of the blades and the frequencies are 0.598,
722 0.647 and 0.684 Hz respectively when Ω= 0.84, 1.27 and 1.68 rad/s, which are 0.4%, 8.1% and 14.7%
723 greater than the frequency of 0.596 Hz when the wind turbine is in the parked condition as tabulated
724 in Table 5. This is because the geometric stiffness arising out of centrifugal stiffening in the flapwise
725 direction can increase the stiffness and vibration frequencies of the blades [10, 33]. In the side-to-side
726 direction, only one peak occurs at 0.156 Hz as shown in Fig. 28(b). This value corresponds to the first
727 vibration frequency of the tower in the side-to-side direction as tabulated in Table 5. Fig. 28 also
728 shows that more energies concentrate in the PSD curves when the blades rotate at a larger velocity,
729 which in turn lead to larger tower responses as shown in Fig. 27.

730

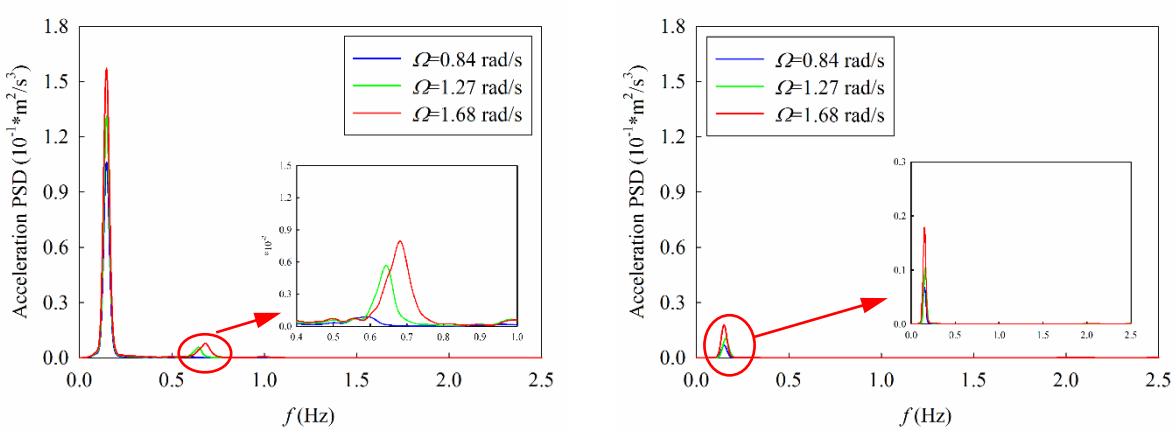

(a) Fore-aft (b) Side-to-side

731 Fig. 28. Fore-aft and side-to-side acceleration PSDs at the tower top under different rotor velocities

732

733 Fig. 29 shows the displacement time histories at the tips of blades in the flapwise direction and Fig. 30
734 shows the edgewise displacements at the tip of Blade 2. As shown in Figs. 29 and 30, both the
735 flapwise and edgewise displacement responses of the blades increase with the increment of the rotor
736 velocity. This is because, as discussed above, the wind loads acting on the blades are larger as shown
737 in Figs. 13(b) and 26, which in turn lead to the larger responses of the blades. Table 9 tabulates the
738 maximum flapwise displacements at each blade tip. The maximum displacements at the tip of Blade 1
739 in the flapwise direction are 1.186, 1.124 and 1.155 m respectively when Ω=0.84, 1.27 and 1.68 rad/s;
740 for Blade 2, the peak values are 1.231, 1.648 and 1.529 m respectively; and the corresponding values
741 are 1.352, 1.773 and 1.984 m respectively for Blade 3. It is interesting to note that, as shown in Fig.
742 30, the displacements at the blade tip in the edgewise direction is not a constant as that shown in Fig.
743 19(b) but increase slightly from about t=200 s especially when Ω=1.68 rad/s. This is because the
744 edgewise wind loads acting on the blades become larger in the time duration of 200-400 s as shown in
745 Fig. 26.

746 Fig. 31 shows the PSDs of the acceleration responses at the tip of Blade 2 in the flapwise and
747 edgewise directions. As shown in Fig. 31(a), the first peak corresponding to the first vibration
748 frequency of the tower (0.154 Hz) is not influenced by the rotor velocity, while the second peak
749 corresponds to the first flapwise pitch vibration mode of the blades and they are 0.549, 0.565 and
750 0.644 Hz respectively when Ω=0.84, 1.27 and 1.68 rad/s; the third peak is related to the first collective

flap vibration mode of the blades, which are 0.598, 0.647 and 0.684 Hz respectively. As shown in Fig. 31(b), only one obvious peak occurs and the frequencies are 0.134, 0.202 and 0.267 Hz respectively, which are the rotor velocities (0.84, 1.27 and 1.68rad/s). Fig. 31 also clearly shows that much more energies are included in the PSD curves with the increment of the rotor velocity, which lead to the larger responses of the blades in both the flapwise and edgewise directions as shown in Figs. 29 and 30.

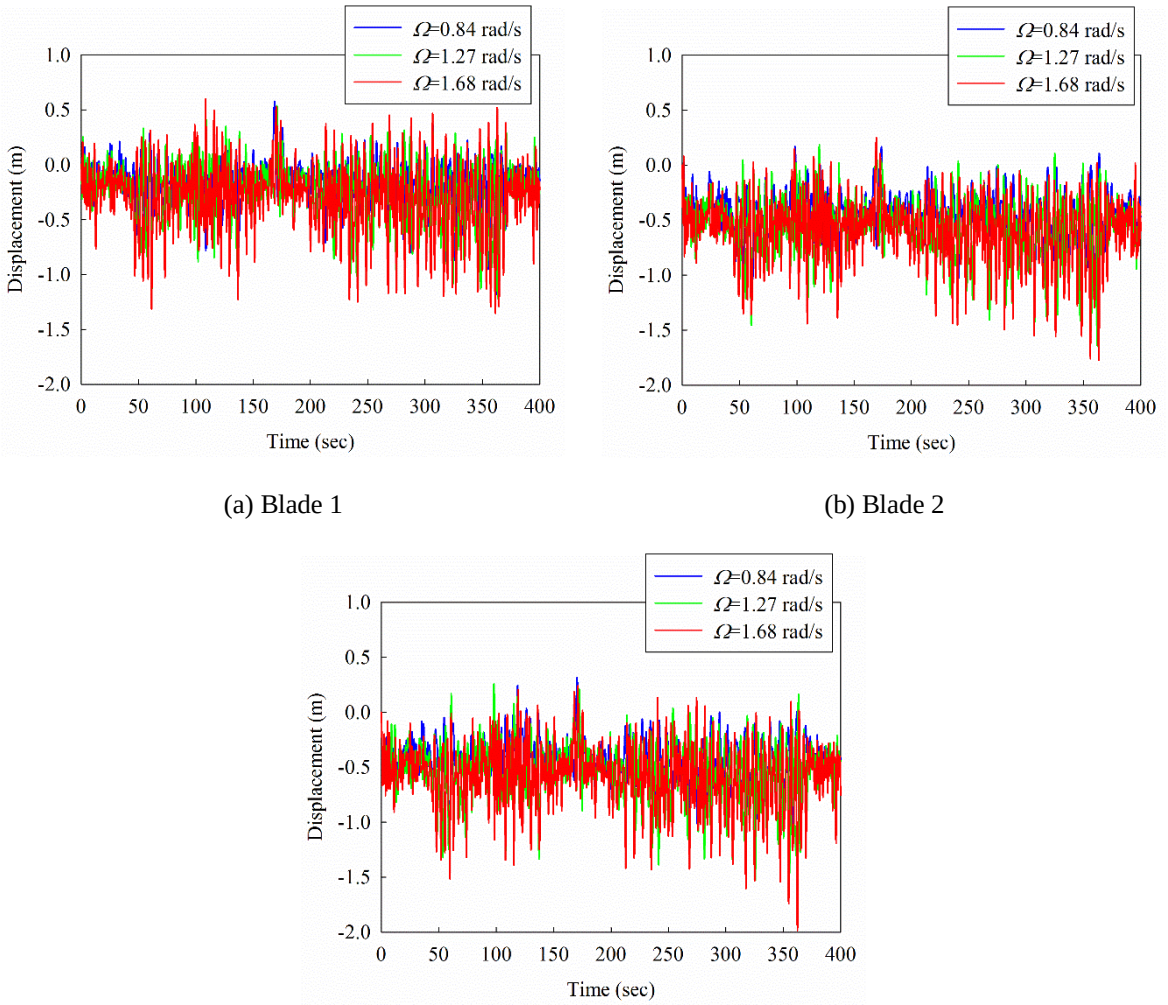

(a) Blade 1

(b) Blade 2

(c) Blade 3

Fig. 29. Flapwise displacement time histories at the blade tips under different rotor velocities

Table 9

Maximum flapwise displacements at the blade tip under different rotor velocities (Unit: m)

Location	Ω=0.84 rad/s	Ω=1.27 rad/s	Ω=1.68 rad/s
Tip of Blade 1	1.186	1.231	1.352
Tip of Blade 2	1.124	1.648	1.773
Tip of Blade 3	1.155	1.529	1.984

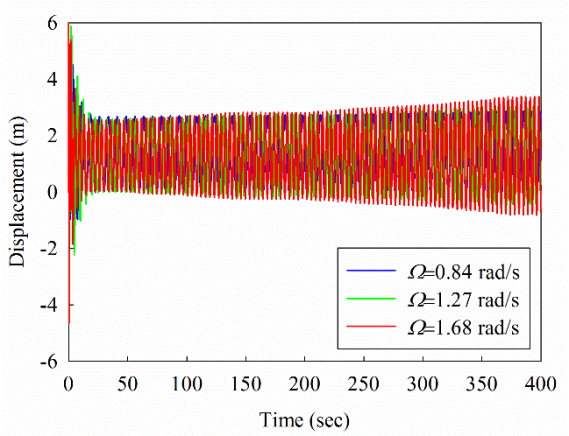

Fig. 30. Edgewise displacement time histories at the tip of Blade 2 under different rotor velocities

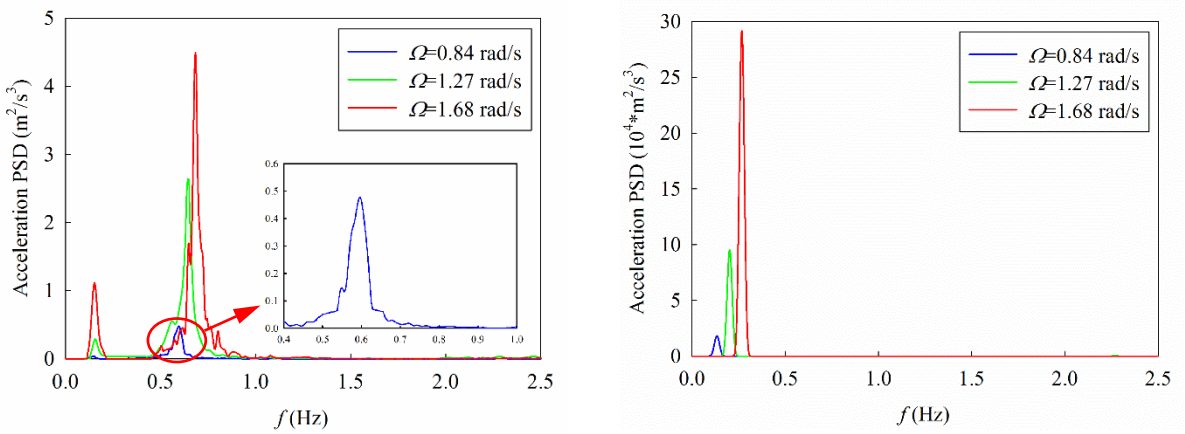

(a) Flapwise (b) Edgewise

Fig. 31. Flapwise and edgewise acceleration PSDs at the tip of Blade 2 under different rotor velocities

5. Conclusions

This paper carries out numerical studies on the dynamic responses of the NREL 5 MW wind turbine subjected to the combined wind and sea wave loadings. The influences of operational conditions, soil-

773 monopile interaction and rotor velocity on the tower and blades are systematically investigated.
774 Numerical results reveal that:
775 (1) The maximum displacements at the top of the tower in the fore-aft and side-to-side directions
776 when the wind turbine rotates with a rotor velocity of 1.27 rad/s are 142% and 222% larger than those
777 when the wind turbine is in the parked condition. The peak flapwise displacement of the blades is
778 about 2.5 times of that of the parked wind turbine. Previous studies by assuming the wind turbines in
779 the parked condition may result in non-conservative structural response estimations and unsafe design
780 of structural components. In the current design codes, safety factors are normally used to account for
781 the uncertainties and variabilities in loads, analysis methods and the importance of structural
782 components for the wind turbines [48, 49]. It will be interesting to develop a uniform safety factor that
783 can be used in the operating response estimation based on the parked results. However, more
784 comprehensive research works are needed.
785 (2) The vibration frequencies of the tower are significantly decreased when SSI is considered, while
786 SSI only marginally affects the natural frequencies of the blades. The out-of-rotor-plane displacement
787 responses of the tower and blades are substantially influenced by SSI. However, SSI has a negligible
788 effect on the displacements of the blades in the edgewise direction.
789 (3) The out-of-rotor-plane displacements of the tower and blades increase with the increment of the
790 rotor velocity. The displacements of the blades in the edgewise direction increase slightly when the
791 rotor velocity becomes larger.
792 It should be noted that wind is the dominant load in the present study by comparing Fig. 9 with Fig.
793 15. Moreover, sea wave is applied near to the bottom of the structure, the influence of the sea wave
794 load on the structural responses is less evident compared to the wind load. When the wind turbine is
795 located in the medium to deep water, the effect of the sea wave load might be obvious. Investigation
796 of the influence of water depth on the structural responses is out of the scope of the present study.
797 Moreover, all the above conclusions are obtained based on the latest NREL 5 MW wind turbine,
798 which is the largest wind turbine in the world currently. These conclusions may only be applicable to
799 this group of wind turbines. To apply the present results in engineering practice and to guide the

800 designs for the whole wind turbine groups (i.e. including the small and medium groups of wind
801 turbines as well), more comprehensive analyses are needed.
802
803 **Acknowledgements**
804 The authors would like to acknowledge the support from Australian Research Council Discovery
805 Early Career Researcher Award DE150100195 for carrying out this research. The first author
806 gratefully acknowledges the financial support from Curtin International Postgraduate Research
807 Scholarship (CIPRS).
808
809 **References**

810 [1] Jonkman J, Butterfield S, Musial W, Scott G. Definition of a 5-MW reference wind turbine for offshore
811 system development Technical Report No NREL/TP-500-38060. Golden, CO: National Renewable Energy
812 Laboratory; 2009.
813 [2] Bazeos N, Hatzigeorgiou G, Hondros I, Karamaneas H, Karabalis D, Beskos D. Static, seismic and stability
814 analyses of a prototype wind turbine steel tower. Eng Struct 2002;24:1015-25.
815 [3] Lavassas I, Nikolaidis G, Zervas P, Efthimiou E, Doudoumis I, Baniotopoulos C. Analysis and design of the
816 prototype of a steel 1-MW wind turbine tower. Eng Struct 2003;25:1097-106.
817 [4] Colwell S, Basu B. Tuned liquid column dampers in offshore wind turbines for structural control. Eng Struct
818 2009;31:358-68.
819 [5] Chen J, Georgakis CT. Tuned rolling-ball dampers for vibration control in wind turbines. J Sound Vib
820 2013;332:5271-82.
821 [6] Bisoi S, Haldar S. Dynamic analysis of offshore wind turbine in clay considering soil-monopile-tower
822 interaction. Soil Dyn Earthquake Eng 2014;63:19-35.
823 [7] Bisoi S, Haldar S. Design of monopile supported offshore wind turbine in clay considering dynamic soil-
824 structure-interaction. Soil Dyn Earthquake Eng 2015;73:103-17.
825 [8] Zuo H, Bi K, Hao H. Using multiple tuned mass dampers to control offshore wind turbine vibrations under
826 multiple hazards. Eng Struct 2017;141:303-15.
827 [9] Hansen M. Aerodynamics of Wind Turbines. 2nd ed. London: Earthscan; 2008.
828 [10] Murtagh PJ, Basu B, Broderick BM. Along-wind response of a wind turbine tower with blade coupling
829 subjected to rotationally sampled wind loading. Eng Struct 2005;27:1209-19.
830 [11] Prowell I, Veletzos M, Elgamal A, Restrepo J. Experimental and numerical seismic response of a 65 kW
831 wind turbine. J Earthquake Eng 2009;13:1172-90.
832 [12] Kjørlaug RA, Kaynia AM. Vertical earthquake response of megawatt-sized wind turbine with soil-structure
833 interaction effects. Earthquake Eng Struct Dyn 2015;44:2341-58.
834 [13] Santangelo F, Failla G, Santini A, Arena F. Time-domain uncoupled analyses for seismic assessment of
835 land-based wind turbines. Eng Struct 2016;123:275-99.
836 [14] Prowell I, Elgamal A, Uang CM, Enrique Luco J, Romanowitz H, Duggan E. Shake table testing and
837 numerical simulation of a utility-scale wind turbine including operational effects. Wind Energy 2014;17:997-
838 1016.
839 [15] Quilligan A, O'Connor A, Pakrashi V. Fragility analysis of steel and concrete wind turbine towers. Eng
840 Struct 2012;36:270-82.
841 [16] Harte M, Basu B, Nielsen SRK. Dynamic analysis of wind turbines including soil-structure interaction. Eng
842 Struct 2012;45:509-18.
843 [17] Fitzgerald B, Basu B. Structural control of wind turbines with soil structure interaction included. Eng Struct
844 2016;111:131-51.
845 [18] Yuan C, Chen J, Li J, Xu Q. Fragility analysis of large-scale wind turbines under the combination of
846 seismic and aerodynamic loads. Renewable Energy. 2017;113:1122-34.

847 [19] Kim DH, Lee SG, Lee IK. Seismic fragility analysis of 5 MW offshore wind turbine. Renewable Energy.
848 2014;65:250-6.
849 [20] Jonkman JM, Buhl Jr ML. FAST User's Guide. Golden, CO: National Renewable Energy Laboratory
850 (NREL); 2005.
851 [21] Damgaard M, Zania V, Andersen LV, Ibsen LB. Effects of soil-structure interaction on real time dynamic
852 response of offshore wind turbines on monopiles. Eng Struct 2014;75:388-401.
853 [22] Kuo YS, Achmus M, Abdel-Rahman K. Minimum embedded length of cyclic horizontally loaded
854 monopiles. J Geotech Geoenviron Eng 2011;138:357-63.
855 [23] Mostafa YE, El Naggar MH. Response of fixed offshore platforms to wave and current loading including
856 soil-structure interaction. Soil Dyn Earthquake Eng 2004;24:357-68.
857 [24] Andersen LV, Vahdatirad M, Sichani MT, Sørensen JD. Natural frequencies of wind turbines on monopile
858 foundations in clayey soils-a probabilistic approach. Comput Geotech 2012;43:1-11.
859 [25] Arany L, Bhattacharya S, Macdonald JH, Hogan SJ. Closed form solution of eigen frequency of monopile
860 supported offshore wind turbines in deeper waters incorporating stiffness of substructure and SSI. Soil Dyn
861 Earthquake Eng 2016;83:18-32.
862 [26] Lombardi D, Bhattacharya S, Wood DM. Dynamic soil-structure interaction of monopile supported wind
863 turbines in cohesive soil. Soil Dyn Earthquake Eng 2013;49:165-80.
864 [27] Bhattacharya S, Adhikari S. Experimental validation of soil-structure interaction of offshore wind turbines.
865 Soil Dyn Earthquake Eng 2011;31:805-16.
866 [28] Hacıefendioğlu K. Stochastic seismic response analysis of offshore wind turbine including fluid-structure-
867 soil interaction. Struct Des Tall Spec Build 2012;21:867-78.
868 [29] Kooijman H, Lindenburg C, Winkelaar D, van der Hooft E. Aero-elastic modelling of the DOWEC 6 MW
869 pre-design in PHATAS DOWEC-F1W2-HJK-01-046/9. 2003.
870 [30] Bi K, Hao H. Using pipe-in-pipe systems for subsea pipeline vibration control. Eng Struct 2016;109:75-84.
871 [31] Burton T, Jenkins N, Sharpe D, Bossanyi E. Wind energy handbook. 2nd ed. John Wiley & Sons; 2011.
872 [32] Det Norske Veritas (DNV). DNV-RP-C205: Environmental conditions and environmental loads. Norway:
873 DNV; 2010.
874 [33] Fitzgerald B, Basu B. Cable connected active tuned mass dampers for control of in-plane vibrations of wind
875 turbine blades. J Sound Vib 2014;333:5980-6004.
876 [34] American Petroleum Institute (API). Petroleum and natural gas industries-specific requirements for
877 offshore structures. Part 4-geotechnical andfoundation design considerations ISO 19901-4:2003 (Modified).
878 2011.
879 [35] Det Norske Veritas (DNV). DNV-OS-J101: Design of offshore wind turbine structures. Copenhagen,
880 Denmark: DNV; 2014.
881 [36] Ashour M, Norris G, Pilling P. Lateral loading of a pile in layered soil using the strain wedge model. J
882 Geotech Geoenviron Eng 1998;124:303-15.
883 [37] Hu WH, Thöns S, Rohrmann RG, Said S, Rücker W. Vibration-based structural health monitoring of a
884 wind turbine system. Part I: Resonance phenomenon. Eng Struct 2015;89:260-72.
885 [38] Valamanesh V, Myers A. Aerodynamic damping and seismic response of horizontal axis wind turbine
886 towers. J Struct Eng 2014;140:04014090.
887 [39] Andersen L. Assessment of lumped-parameter models for rigid footings. Comput Struct 2010;88:1333-47.
888 [40] Chopra AK. Dynamics of Structures. 4th ed. New Jersey: Prentice Hall; 2012.
889 [41] Benowitz BA, Deodatis G. Simulation of wind velocities on long span structures: a novel stochastic wave
890 based model. J Wind Eng Ind Aerodyn 2015;147:154-63.
891 [42] Huang G, Liao H, Li M. New formulation of Cholesky decomposition and applications in stochastic
892 simulation. Probab Eng Mech 2013;34:40-7.
893 [43] Hao H, Oliveira C, Penzien J. Multiple-station ground motion processing and simulation based on
894 SMART-1 array data. Nucl Eng Des 1989;111:293-310.
895 [44] Bi K, Hao H. Modelling and simulation of spatially varying earthquake ground motions at sites with
896 varying conditions. Probab Eng Mech 2012;29:92-104.
897 [45] Hasselmann K, Barnett T, Bouws E, Carlson H, Cartwright D, Enke K, et al. Measurements of wind-wave
898 growth and swell decay during the Joint North Sea Wave Project (JONSWAP). Hamburg: Deutches
899 Hydrographisches Institut; 1973.
900 [46] Sorensen RM. Basic coastal engineering. New York: Springer Science & Business Media; 2005.
901 [47] Staino A, Basu B. Dynamics and control of vibrations in wind turbines with variable rotor speed. Eng
902 Struct 2013;56:58-67.
903 [48] IEC 61400-1. Wind turbines-Part 1: Design requirements. 3rd ed. Geneva, Switzerland: International
904 Electrotechnical Commission; 2005.
905 [49] IEC 61400-3. Wind turbines-Part 3: Design requirements for offshore wind turbines. 1st ed. Geneva,
906 Switzerland: International Electrotechnical Commission; 2009.